NeuroImage 209 (2020) 116486

Contents lists available at ScienceDirect

NeuroImage

journal homepage: www.elsevier.com/locate/neuroimage

A novel approach to localize cortical TMS effects

Konstantin Weise [a,b,*,1], Ole Numssen [c,1], Axel Thielscher [d,e], Gesa Hartwigsen [c,2], Thomas R. Knösche [a,f,2]

[a] Methods and Development Group "Brain Networks", Max Planck Institute for Human Cognitive and Brain Sciences, Stephanstr. 1a, 04103, Leipzig, Germany
[b] Technische Universität Ilmenau, Advanced Electromagnetics Group, Helmholtzplatz 2, 98693, Ilmenau, Germany
[c] Lise Meitner Research Group "Cognition and Plasticity", Max Planck Institute for Human Cognitive and Brain Sciences, Stephanstr. 1a, 04103, Leipzig, Germany
[d] Danish Research Centre for Magnetic Resonance, Centre for Functional and Diagnostic Imaging and Research, Copenhagen University Hospital Hvidovre, Denmark
[e] Technical University of Denmark, Center for Magnetic Resonance, Department of Health Technology, Kongens Lyngby, Denmark
[f] Technische Universität Ilmenau, Institute of Biomedical Engineering and Informatics, Gustav-Kirchhoff-Straße 2, 98693, Ilmenau, Germany

ARTICLE INFO

Keywords:
Brain mapping
Finite element analysis
Motor cortex
Transcranial magnetic stimulation
Uncertainty and sensitivity analysis
Motor threshold

ABSTRACT

Despite the widespread use of transcranial magnetic stimulation (TMS), the precise cortical locations underlying the resulting physiological and behavioral effects are still only coarsely known. To date, mapping strategies have relied on projection approaches (often termed "center of gravity" approaches) or maximum electric field value evaluation, and therefore localize the stimulated cortical site only approximately and indirectly. Focusing on the motor cortex, we present and validate a novel method to reliably determine the effectively stimulated cortical site at the individual subject level. The approach combines measurements of motor evoked potentials (MEPs) at different coil positions and orientations with numerical modeling of induced electric fields. We identify sharply bounded cortical areas, around the gyral crowns and rims of the motor hand area, as the origin of MEPs and show that the magnitude of the tangential component and the overall magnitude of the electric field are most relevant for the observed effect. To validate our approach, we identified the coil location and orientation that produces the maximal electric field at the predicted stimulation site, and then experimentally show that this location produces MEPs more efficiently than other tested locations/orientations. Moreover, we used extensive uncertainty and sensitivity analyses to verify the robustness of the method and identify the most critical model parameters. Our generic approach improves the localization of the cortical area effectively stimulated by TMS and may be transferred to other modalities such as language mapping.

1. Introduction

Transcranial magnetic stimulation (TMS) is increasingly being used to modulate motor and cognitive functions in the human brain. An important application of this technique is mapping structure-function relationships (see Bestmann, 2008; Bestmann and Feredoes, 2013; Hallett, 2000; Sandrini et al., 2011; Siebner et al., 2009 for review). To understand brain physiology and structure-function relationships, it is essential to exactly know which part of the brain is activated by TMS and precisely localize it at the individual subject level. Such mappings are not only of fundamental neuroscientific interest, but also have practical clinical relevance, for example in the context of pre-surgical mapping for counseling and planning of tumor resections or epilepsy surgeries. In a typical mapping study, the TMS coil is systematically moved over different positions and/or orientations while certain behavioral or physiological variables (e.g., the degree of speech impairment or the amplitude of motor evoked potentials (MEPs)) are measured (Picht, 2014). The coil position/orientation producing the strongest effect is then used as a proxy for the brain structures underlying the targeted effects, either in a simple way by direct projection onto the cortical surface (Krieg et al., 2014) or in a more sophisticated way by calculating the induced electric fields (Tarapore et al., 2013). Rather than picking the grid position with the strongest MEPs, this is usually done by determining the "center of gravity" of the MEP responses measured across the complete grid in order to gain robustness to measurement noise (e.g., Classen et al., 1998). However, this approach has some shortcomings. First, its capability to

* Corresponding author. Max Planck Institute for Human Cognitive and Brain Sciences, Stephanstr. 1a, 04103 Leipzig, Germany.
E-mail addresses: kweise@cbs.mpg.de (K. Weise), numssen@cbs.mpg.de (O. Numssen).
[1] Shared first authorship.
[2] Shared senior authorship.

https://doi.org/10.1016/j.neuroimage.2019.116486
Received 27 March 2019; Received in revised form 12 December 2019; Accepted 19 December 2019
Available online 23 December 2019

unambiguously determine the location and orientation of activated neural structures is limited. Even if the coil configuration associated with the optimal effect can be accurately identified, it generates electric fields in a wide range of neural structures, such as radial cells in adjacent sulcal walls and tangential structures (e.g., axons) in gyral crowns. Therefore, the location of the electric field maximum does not necessarily coincide with the location of the functionally involved neurons driving the effect. Second, as the search space has at least three dimensions (two for the position on the head surface, one for coil orientation), accurate mapping may require a very large number of TMS pulses to avoid undersampling. Consequently, previous studies remain controversial on fundamental aspects of the physiological TMS effects and their localization on the cortical surface. For instance, it is still unclear which part of the primary motor cortex is effectively stimulated by the TMS pulse (see Bungert et al., 2017; Laakso et al., 2018; Fox et al., 2004; Krieg et al., 2013), precluding strong conclusions on the cortical origin of the TMS effect. In particular, previous studies remain controversial with respect to the contribution of the gyral crowns and sulcal walls in the primary motor cortex (see Fox et al., 2004; Bungert et al., 2017; Opitz et al., 2013; Laakso et al., 2018; Krieg et al., 2013).

Resolving these limitations and establishing a link between coil position and location and size of the affected cortical area in three dimensions (i.e., also in depth) is not trivial. It requires detailed knowledge of the electric field pattern at the individual subject level, biophysically motivated hypotheses on the mechanism of action by which the electric field causes neural excitation, and formal statistical testing to demonstrate the validity of the obtained results.

The induced electric field distribution depends on multiple stimulation parameters such as intensity, location, and orientation of the TMS coil. The complex geometry of the individual brain (Thielscher et al., 2011) and several biophysical parameters, such as tissue conductivity and fractional anisotropy, are also involved. Numerical modeling of the induced electric field is increasingly being used to address these issues (Bestmann, 2015; Thielscher et al., 2011, 2015), but has not become a standard procedure in medical and scientific applications so far. In particular, calculations based on subject-specific head meshes have improved our understanding of the impact of individual head anatomy on field distributions (Datta et al., 2010; Opitz et al., 2011, Opitz et al., 2013, 2014; Thielscher et al., 2011; Wenger et al., 2015; Wolters et al., 2006; Vorwerk et al., 2014). As such, numerical field calculations using anatomically detailed head models may assist the neurobiological interpretation of TMS effects and aid the localization of the effectively stimulated cortical area that underlies the observed physiological or behavioral effect (see Hartwigsen et al., 2015; Bungert et al., 2017). However, since a TMS pulse induces a distributed electric field over an extended part of the cortex, it is difficult to determine the location of neural activation, even if the field is computed in a reliable way. Moreover, any approach that makes use of field models has to account for model errors. On the one hand, systematic errors originate, for example, from inaccurate meshing, solving, and post-processing. The impact of these error sources can be controlled for by an appropriate validation of the numerical accuracy of the implemented pipeline (Saturnino et al., 2019b). Segmentation errors are another source of inaccuracies in the simulated fields (Puonti et al., 2019b; Huang et al., 2019). In fact, the amount of differences in the automated segmentations created by different pipelines have between shown to directly relate to the amount of differences in the field estimates (Puonti et al., 2019a). It is thus important to minimize segmentation errors by using appropriate input images (a combination of T1-and T2-weighted structural MR images; Nielsen et al., 2018) and to visually evaluate the anatomical accuracy of the final head mesh in the region of interest (ROI). On the other hand, errors may also originate from uncertainties in model parameters, such as the ohmic tissue conductivity or the fractional anisotropy (Weise et al., 2015; Saturnino et al., 2019), which are only coarsely known. Unfortunately, these errors cannot be avoided and have to be considered during the development of new methods. Finally, a localization approach has to be able to deal with uncertainties caused by the limited knowledge of how the induced field acts on different neuron types. Recently, field calculations have been combined with microscopic neural models based on accurate reconstructions from histology (Seo et al., 2017; Aberra et al., 2018). However, to a large extent, validation of these models is still missing and the conclusions strongly depend on specific model details, such as the types of neural elements included. Consequently, the results of previous studies are not consistent and do not provide reliable conclusions yet.

In this study, we introduce a novel TMS mapping approach that links biophysical modeling of the induced electric field with physiological measurements within a principled statistical testing framework to determine the effectively stimulated cortical area at the individual subject level. Our approach is based on the assumption of a unique functional relationship between the observed physiological TMS effect and the electric field induced at the cortical location underlying this effect. Moreover, we assume that the experimental effects can be explained by activity in a relatively focal single cortical patch. Given an experimental effect that linearly or non-linearly scales with stimulation intensity, one can assume that this effect also scales with the degree of excitation of the specific neuronal population, which is functionally linked to it. Hence, the functional relationship between the electric field component that coincides spatially and orientation-wise with this population, and the observed effect, should be invariant across experimental conditions, that is, different orientations and positions of the TMS coil. Consequently, the effectively stimulated cortical area can be identified by determining the brain area in which the induced field shows a stable functional relationship between the measured effect across conditions. Note that this area does not have to coincide with the field maximum. Similar but more restricted localization approaches have been used in previous studies. For instance, targeting the hand area of the primary motor cortex, Bungert et al. (2017) employed a statistical approach based on the experimentally determined motor threshold (MT) at different coil orientations. Laakso et al. (2018) used a similar strategy but investigated the influence of different coil positions while keeping the orientation constant. These studies demonstrate the principal rationale to localize the effectively stimulated cortical area using the functional relationship between calculated fields and the observed effects. However, they remain restricted in several important aspects. First, the ability for a precise functional localization at the single-subject level was not demonstrated. Second, it remains unknown how many experimental conditions are needed to achieve a satisfying localization result and how these coil positions and orientations should be chosen. Third, the robustness of these approaches to uncertainties in tissue conductivity was not examined. Finally, all of the aforementioned studies lack experimental validation.

Our novel approach differs from prior work in two important aspects regarding localization at the single-subject level. First, it fully utilizes information from multiple TMS conditions with different coil positions and orientations. Second, instead of relying on motor threshold, we exploit entire input-output curves (I/O curves; relationship between stimulator intensity and MEP amplitude; see Fig. 1). We show that our method provides a means of localizing the individual cortical location that is responsible for the observed motor output with high precision. Furthermore, we confirm the validity of this localization by numerically optimizing the individual TMS coil position and orientation such that the maximum of the induced electric field coincides with the identified cortical location, and then showing in an additional experiment that these coil positions and orientations do indeed produce lower MTs than other tested coil configurations. We demonstrate its stability and robustness using comprehensive permutation tests and a rigorous uncertainty and sensitivity analysis based on the generalized polynomial chaos (gPC) approach (Le Maitre and Knio, 2010). To account for the limited knowledge of the neural structures affected from TMS, we tested several components of the induced field and consistently found the magnitude of the tangential field component and the overall field

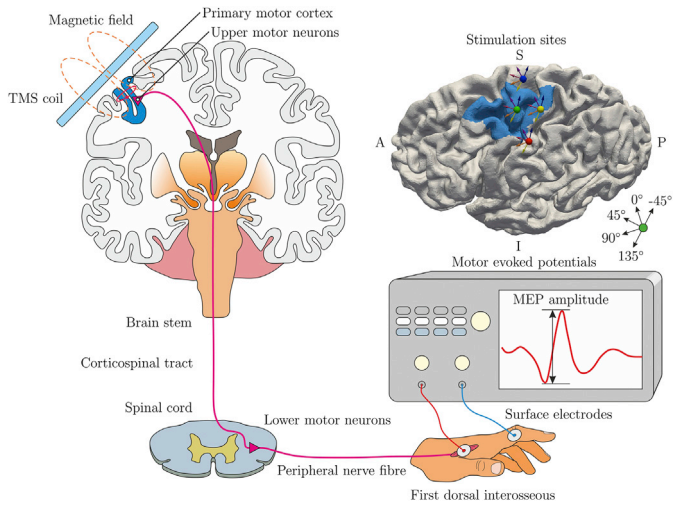

Fig. 1. Schematic representation of the experimental procedure of the TMS experiments. Top left: the TMS coil is located tangentially to the scalp over the primary motor cortex (M1). A time changing current in the coil generates a time changing magnetic field, which induces an electric field in the brain. This depolarizes the upper motor neurons with corticospinal efferents. Bottom: action potentials from the upper motor neurons excite the lower motor neurons in the spinal cord, evoked action potentials travel through the peripheral nerves to the first dorsal interosseous (FDI) of the hand. Sum potentials (motor-evoked potentials, MEP) are recorded from hand muscles using a classical belly tendon montage, i.e., between the dorsal interosseous and proximal interphalangeal joint of the index finger. Top right: example cortical surface with region of interest (blue), showing positions of the coil centers (colored spheres) and the coil orientations (arrows) for the 20 experimental conditions.

magnitude to be the relevant quantities for modulating the observed effect. Importantly, we demonstrate that unique results can be obtained with relatively few measurements and indicate how the respective coil positions and orientations should be chosen. Our approach improves the localization of effectively stimulated areas during TMS. While demonstrated for the motor cortex, our approach is generic and can be applied to mapping procedures in other domains as long as our assumption of a single relevant cortical site is not violated. However, the approach can in principle be extended to multiple relevant cortical sites, as it is expected, for example, in case of language mapping.

2. Materials and methods

We developed a novel framework to localize the neuronal populations that are responsible for the effects of TMS by combining physiological responses with numerical modeling. We applied this to primary motor cortex stimulation and electrophysiological measurements of muscle activation. First, we describe the experimental design to elicit and measure MEPs (Section 2.1). Second, we show how to calculate the TMS-induced electric field distribution in the subjects' heads (Section 2.2). This involves models for the head, the TMS coils, as well as the differential equations numerically solved to determine the electric field inside the brain. Third, we present a new measure to quantify the correlation between the induced electric field and the physiological effect, the *congruence factor*. Locations with high congruence are likely to house neural populations that are linked to the observed MEP (Section 2.3). We then show how the results are analyzed in terms of their sensitivity towards uncertain model parameters such as the electrical conductivity of the brain tissues and the measured MEPs using a generalized polynomial chaos (gPC) approach (Section 2.4). Finally, the validation procedure for our results is outlined (Section 2.5).

2.1. TMS experiments

The experimental setup is shown in Fig. 1. Fifteen healthy, right-handed participants (seven female, age 22–34 years) with a mean laterality index of 92.93 (SD = 10.66) according to the Edinburgh Handedness Inventory were recruited (Oldfield, 1971). Subject inclusion was in accordance with the published safety guidelines for TMS studies (Rossi et al., 2009; Rossini et al., 2015). Written informed consent was obtained from all participants prior to the examination. The study was performed according to the guidelines of the Declaration of Helsinki and approved by the local Ethics committee of the Medical Faculty of the University of Leipzig.

TMS pulses were applied with a MagPro X100 stimulator (MagVenture, firmware Version 7.1.1) and CB-60 figure-of-eight coils, guided by a neuronavigation system (software: Localite, Germany, Sankt Augustin; camera: Polaris Spectra, NDI, Canada, Waterloo).

MEPs were recorded from the subjects' right index finger with one surface electrode positioned over the first dorsal interosseous (FDI) muscle belly and one at the proximal interphalangeal joint (PIP). The electrodes were connected to a patient amplifier system (D-360, DigitimerLtd., UK, Welwyn Garden City; bandpass filtered from 10 Hz to 2 kHz), which in turn was connected to a data acquisition interface (Power1401 MK-II, CED Ltd., UK, Cambridge, 4 kHz sampling rate). Electromyography recording was performed with Signal (CED Ltd., version 4.11).

Localization of the initial MEP target location was guided by individually transformed M1 coordinates based on the standardized group coordinates from a meta-analysis (Mayka et al., 2006). These coordinates were transformed to the individual subject's space by using the inverse of the normalization transformation in SPM (Penny et al., 2007; https://www.fil.ion.ucl.ac.uk/spm/). With a standard threshold hunting procedure, we manually determined the resting motor threshold (rMT) and the corresponding coil position and orientation for each subject. As this coil orientation usually is about 45° towards the *fissura longitudinalis*, we call this $MT_{45°}$, the corresponding coil configuration $M1_{45°}$, and refer to the coil angle as 45° in the following (Brasil et al., 1992; Mills et al., 1992). $MT_{45°}$ was defined as the minimum stimulator intensity which evoked MEPs with an amplitude of at least 50 μV in at least 5 out of 10 consecutive TMS pulses (Pascual-Leone and Torres, 1993; Rothwell et al., 1999; Conforto et al., 2004).

In relation to $M1_{45°}$, five additional conditions, shown in Fig. 2a, with different coil positions and orientations (see Fig. 2a) were defined in the following way. In Experiment I, the TMS coil was located over M1 and 2 cm posterior (P). At both sites, three coil orientations with respect to $M1_{45°}$ were investigated, namely $M1_{0°}/P_{0°}$ (−45° from $M1_{45°}$), $M1_{45°}/P_{45°}$, and $M1_{90°}/P_{90°}$ (+45° from $M1_{45°}$), resulting in six experimental conditions.

Experiment II included three of the subjects from Experiment I and the number of conditions was increased to further investigate the influence of different coil positions and orientations on the identification of the relevant cortical site. In addition to M1 and P, two more coil positions were included: 2 cm inferior and 2 cm superior to M1, respectively (Fig. 2b). For each position, the number of coil orientations was increased to 5 (−90°, −45°, 0°, 45°, 90°) with respect to $M1_{45°}$, resulting in 20 experimental conditions.

In both experiments, single biphasic pulses with an inter stimulus interval (ISI) of 5 s (Experiment I) or 4 s (Experiment II) were applied for each condition. The coil positions/orientations were recorded by the neuronavigation system. The MEPs were lowpass filtered with a 6th order Butterworth filter with a cutoff frequency of 500 Hz. Afterwards, the peak-to-peak amplitudes of the MEPs were calculated in a time window of 18–35 ms after the TMS pulse (see Fig. 3a for an example MEP). Stimulator intensities were chosen to sample the complete I/O curve for each experimental condition, unless maximal stimulator output was reached before (Fig. 3b). Intensity was increased in steps of 2% stimulator output (MSO), or 1% respectively for intensity ranges of high

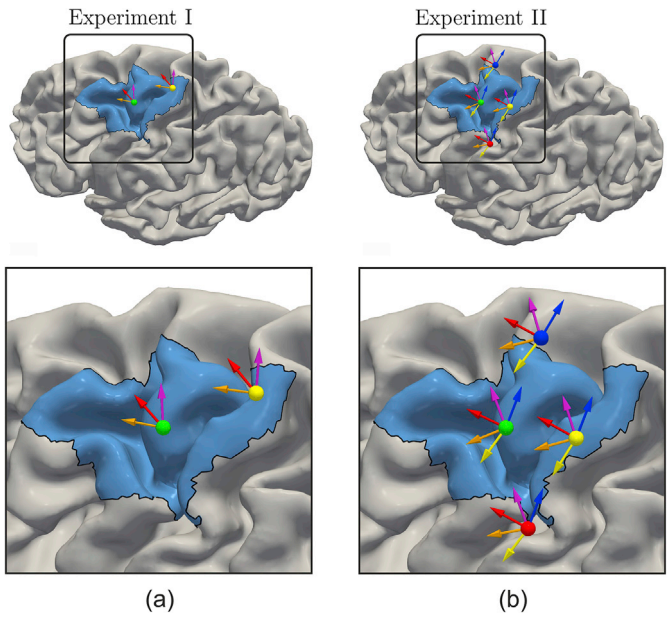

Fig. 2. Coil positions and orientations used in (a) Experiment I and (b) Experiment II. The locations are exemplarily shown for subject Sub08. The number of experimental conditions increased from six to 20. The blue area is the region of interest, comprised of the somatosensory cortex (BA 1, BA 3), M1 (BA 4), and the dorsal part of the premotor cortex (BA 6).

I/O gradients (cf. Bungert et al., 2017). For each intensity, 3–5 TMS pulses were delivered to determine an average MEP amplitude. Trials with deviations in coil position of ±3 mm and orientation of ±5° with respect to each axis were removed. A typical set of data points is shown in Fig. 3b (blue dots). Thereafter, a sigmoidal function was fitted in a least-square sense:

$$s_i(x) = \frac{a_i}{1 + e^{-b_i(x - x_{0,i})}}, \tag{1}$$

where a_i is the saturation amplitude, b_i the slope, and $x_{0,i}$ is the location of the turning point on the abscissa. If only a part of the I/O curve could be determined experimentally, a sigmoidal function could not be reliably fitted and an exponential or linear function was used instead. The selection of the optimal model was performed using the Akaike information criterion (AIC, Akaike, 1974). The procedure was repeated for all experimental conditions (i.e., for different coil positions and orientations) in a pseudo-randomized order.

2.2. Numerical simulations of the induced electric field

The calculations of the electric field were conducted with SimNIBS v2.0 (Thielscher et al., 2015) using high-resolution anisotropic finite element models (FEMs). An example is shown for one subject in Fig. 4. The individual head models were generated from MRI data using the pipeline described in Windhoff et al. (2013), employing FreeSurfer (http://surfer.nmr.mgh.harvard.edu/, Dale et al., 1999; Fischl et al., 1999) and FSL (https://fsl.fmrib.ox.ac.uk/fsl/fslwiki/FSL, Woolrich et al., 2009; Smith et al., 2004; Jenkinson et al., 2012). The head models were composed of ~$1.3{\cdot}10^6$ nodes and ~$7{\cdot}10^6$ tetrahedra with an average volume of ~0.28 mm^3 in the cortex. T1 and T2 images were used for segmenting the main tissues of the head: scalp, skull, grey matter (GM), white matter (WM), and cerebro-spinal fluid (CSF). Diffusion weighted images were used to reconstruct the conductivity tensors in the WM using the volume normalized mapping approach (Güllmar et al., 2010). To this end, the following structural images were acquired with a 3 T MRI scanner (Siemens Verio or Skyra) and a 32 channel head coil: (i) T1-weighted: MPRAGE with 176 sagittal slices, matrix size = 256 × 240, voxel size = 1 × 1 × 1 mm^3, flip angle 9°, TR/TE/TI = 2300/2.98/900 ms (repetition, spin echo, inversion Time), (ii) T2-weighted: 192 sagittal slices, matrix size = 256 × 258, voxel size = 0.488 × 0.488 × 1 mm^3, flip angle 120° TR/TE = 5000/395 ms (iii) diffusion MRI 67 axial slices, matrix size 128 × 128, voxel size 1.71875 × 1.71875 × 1.7 mm^3, TE/TR 80/7000 ms, flip angle 90°, 67 diffusion directions, b-value 1000 s/mm^3. An additional b0 image with reversed encoding direction was acquired and used during the calculation of the conductivity sensors for eddy current correction and distortion correction. The T1 image was also used for neuronavigation during TMS. If adequate scans already existed for the subjects in the image database (age less than 1 year), these scans were utilized.

All TMS coils were individually modelled by magnetic dipoles based on X-ray images. Coil wiring differences (shifts of several millimeters and tiltings of about 2–5°) were observed and accounted for. Each coil model consisted of ~4500 magnetic dipoles, situated in 5 layers in the coil plane. Their magnitudes were determined from the enclosed current. The dipole models were compared to detailed current density based FEM models using Comsol Multiphysics v4.4 (COMSOL, Inc., Burlington, MA, USA) and yielded magnetic field errors of <0.1% at a distance of 15 mm.

The magnetic field generated by the coil determines the primary electric field $\mathbf{E}_p$. It was precomputed in terms of the magnetic vector potential $\mathbf{A}$ and then mapped to the FEM nodes for each coil configuration. The primary electric field is then given by $\mathbf{E}_p = -j\omega\mathbf{A}$, where $\omega = 2\pi f$ is the angular frequency of the biphasic TMS pulse. The electric potential φ in the nodes is calculated by solving the Laplace equation $\nabla \cdot ([\sigma]\nabla\varphi) = 0$ using FEM, considering anisotropic conductivity tensors $[\sigma]$ inside each element together with the boundary conditions given by the law of current conservation $\nabla \cdot \mathbf{J} = -[\sigma](j\omega\mathbf{A} + \nabla\varphi) = 0$. After calculating the secondary electric field $\mathbf{E}_s = -\nabla\varphi$, the total induced electric field is given by $\mathbf{E} = \mathbf{E}_p + \mathbf{E}_s = -j\omega\mathbf{A} - \nabla\varphi$. The conductivity values for the five examined tissues ($\sigma_{Scalp} = 0.465$ S/m, $\sigma_{Skull} = 0.01$ S/m, $\sigma_{GM} = 0.275$ S/m, $\sigma_{WM} = 0.126$ S/m, $\sigma_{CSF} = 1.654$ S/m) were taken

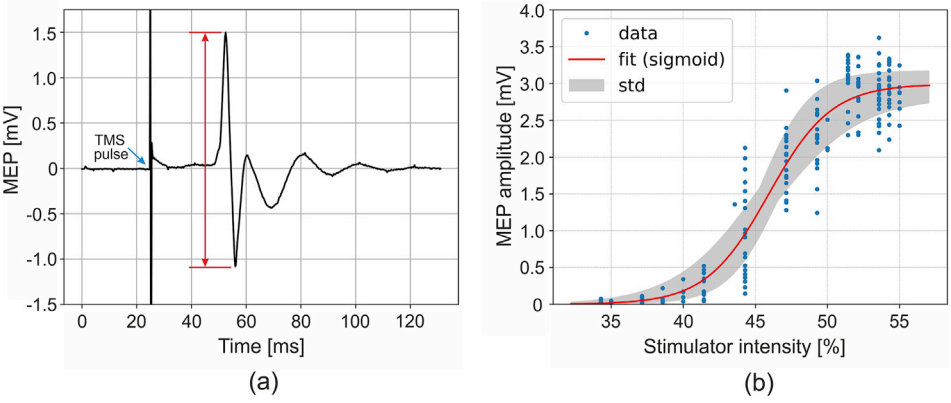

Fig. 3. (a) Measured motor evoked potential (MEP) showing the stimulation artifact (blue arrow) and the peak-to-peak amplitude (red arrow). (b) I/O curve characterizing the MEP amplitudes as function of the stimulator intensity for one experimental condition. Blue dots: MEP amplitudes for the different stimulator intensities. Red curve: fitted analytical function. Depending on the best Akaike information criterion (AIC), MEP amplitudes were fitted to sigmoidal, exponential or linear functions (presented example: sigmoid function). Black lines: possible I/O curves resulting from uncertainty in the experimental data.

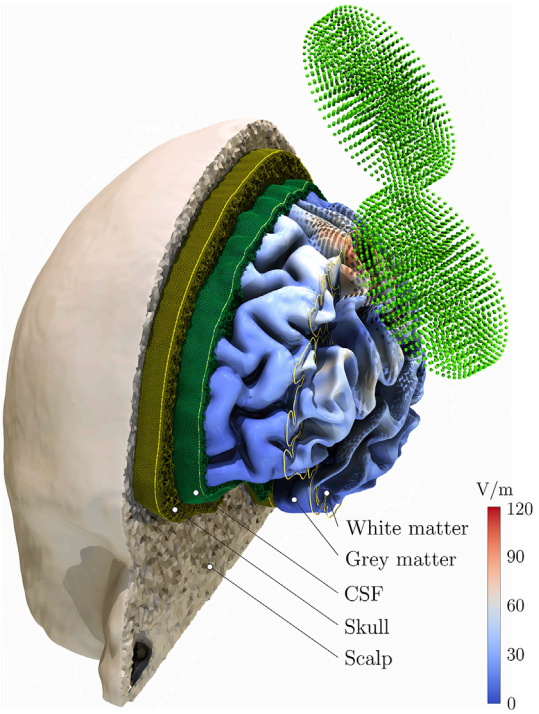

Fig. 4. Example of the realistic anisotropic head model of one subject, used for the numerical simulations of the induced electric field. The model consists of $1.26 \cdot 10^6$ nodes and $7.12 \cdot 10^6$ tetrahedra. The TMS coil is modelled using 4440 magnetic dipoles (green spheres) with optimized dipole moments located in five layers. The grey matter surface is color coded with the magnitude of the induced electric field for 1 A/µs intensity.

from Thielscher et al. (2011) and Wagner et al. (2004). A more detailed description of the FEM solver is given in Windhoff et al. (2013, supplemental material) and Saturnino et al. (2019b).

Individual coil positions and orientations relative to the subject's head were saved by the neuronavigation system for each TMS pulse. During the experiment, we placed the coil such that it touched the scalp (with a small bias due to the hair layer) in each subject. In some cases, we observed slight distances between coil and head surface of about 0.5–2 mm in the subsequent modeling step. We shifted the coil position perpendicularly to the head surface to reduce these small errors, which were presumably caused by uncertainties in the neuronavigation and the head surface reconstruction. These coil configurations were used for electric field calculations in SimNIBS. A ROI was defined with Freesurfer covering the somatosensory cortex (BA 1, BA 3), primary motor cortex M1 (BA 4), and the dorsal part of the premotor cortex (BA 6) and a mask was created for the Freesurfer average template and transformed to each individual subject's brain.

The following analyses were performed on the midlayer between the outer surfaces of the GM and WM compartments to avoid boundary effects of the electric field due to conductivity discontinuities. The electric field interpolation followed the procedure described in Saturnino et al. (2019b), using the super-convergent patch recovery method (Zienkiewicz and Zhu, 1992) to determine the electric field at the nodes within grey matter and then computed the electric field at the grey matter center using linear interpolation. Fig. 5 shows the magnitude $|\mathbf{E}|$, the normal component $E_\perp$ and the magnitude of the tangential component $|\mathbf{E}_{||}|$ of the electric field at the midlayer surface for three different coil positions and orientations in one exemplary subject. The different electric field distributions are shown in the highlighted ROI for the different experimental conditions.

2.3. Determining the site of effective stimulation

The core concept of the proposed method is illustrated in Fig. 6. We assume that at the site of activation the relationship between electric field and MEP is stable, i.e., the same electric field strength always evokes the same behavioral output, independent of the location or orientation of the TMS coil. Furthermore, we assume that exactly one focal cortical area at M1 is functionally relevant for evoking MEPs. Exploiting these assumptions, the site of effective stimulation can be pinpointed by calculating *cortical I/O curves* that represent the relationship between the electric field in the cortex and the resulting MEP. At the functionally relevant cortical site of activation, the cortical I/O curves of all conditions have to be similar. Practically, this was achieved by transforming the measured I/O curves for each condition (representing the relationship between stimulator intensity in percent of maximal stimulator output, %MSO, and MEP amplitude) to E-MEP curves (representing the relationship between the electric field at a particular cortical location and the respective MEP amplitude). The electric field distribution throughout the brain was computed as a function of %MSO using the numerical techniques described above, taking 100% MSO as corresponding to a maximal change of the coil current of 143 A/µs for the specific stimulator-coil combination. Due to the linear relationship between the electric field strength and the stimulator intensity, the E-MEP curves are shifted, horizontally-scaled versions of the measured I/O curve, with different shift and scale parameters in each position. Hence, the function types of each I/O curve and their corresponding E-MEP curves are similar (i.e., sigmoidal, exponential, or linear). E-MEP curves can be determined for all different components of the electric field vector ($|\mathbf{E}|$, $E_\perp$, $|\mathbf{E}_{||}|$) or, in principle, any other derived quantities thereof. This approach allows the computation of a position-wise *congruence factor* $c(\boldsymbol{r})$, which quantifies the similarity between the E-MEP curves of the different experimental conditions.

The agreement between different I/O curves was quantified by computing the inverse variance of the *optimal shifts* τ_i with $i = 1 \ldots N_c$ of the N_c I/O curves across the experimental conditions.

$$c(\boldsymbol{r}) = \left(\frac{1}{N_c} \sum_{i=1}^{N_c} \frac{(\bar{\tau}(\boldsymbol{r}) - \tau_i(\boldsymbol{r}))^2}{\bar{E}^2(\boldsymbol{r})} \right)^{-1} \tag{2}$$

The congruence factor $c(\boldsymbol{r})$ was calculated for each element in the cortical ROI by determining the inverted variance of the τ_i, additionally weighted by the average electric field magnitude (or the normal component or the magnitude of the tangential component) squared at this location: $\bar{E}^2(\boldsymbol{r})$. Hence, the congruence factor quantifies a relative similarity between the observations in the different experimental conditions, independent of the scale of the electric field. Higher similarity between curves leads to higher inverse variance. The optimal shifts τ_i were obtained by determining the individual locations where the overlap against a reference curve, e.g. the first E-MEP curve, is maximized. As a result, the problem of determining the congruence factor turns into many optimization problems calculating the shifts τ_i for each condition and in each element in the ROI:

$$\min_{\tau_i} \left\| s_{REF}^{\cdot}(E(\boldsymbol{r})) - s_i^{\cdot}(E(\boldsymbol{r}) - \tau_i) \right\|_2 \tag{3}$$

Where $s_{REF}^{\cdot}$ and $s^{\cdot}$ denote the reference and one of the I/O curves the shift is calculated for, respectively. This method is very general, as it is independent of the involved function types.

It should be noted that the direction of the normal component of the electric field along the pyramidal apical dendrites is likely to have an influence on the activation of the neurons. For a particular voxel, the normal field component might point outwards (positive) for some stimulation conditions, and inwards (negative) for others. As a consequence, the curves for the negative and positive ranges must be analyzed *separately* and their respective congruencies must be merged afterwards. A

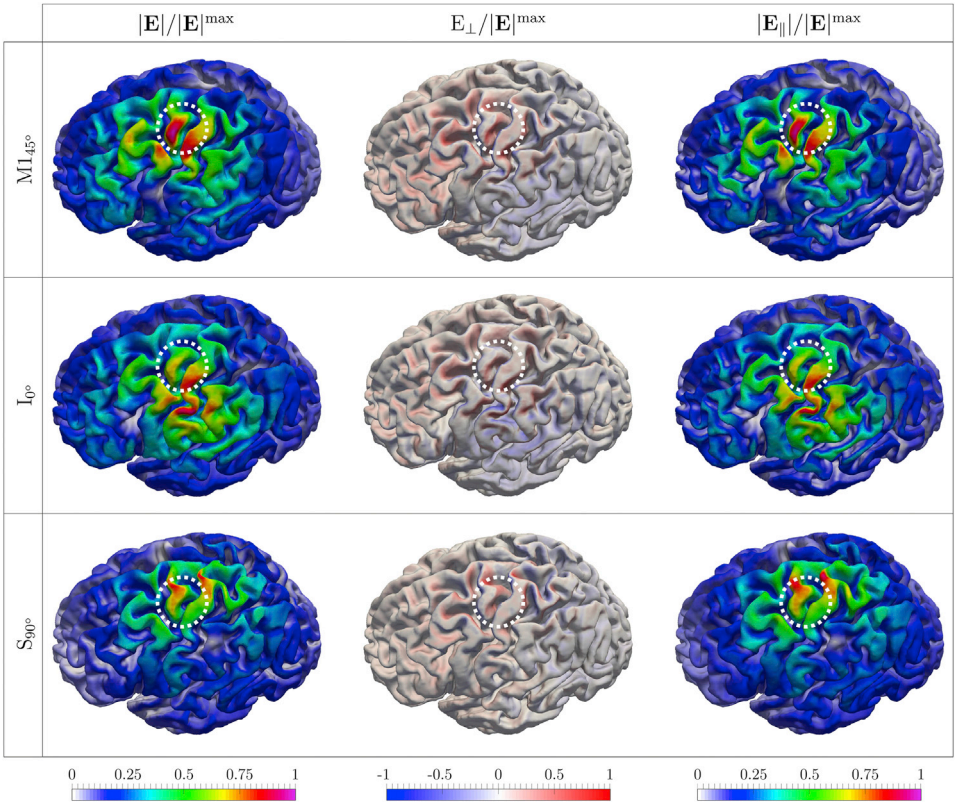

Fig. 5. Three electric field distributions, i.e., the overall magnitude of the electric field $|\mathbf{E}|$, the normal component $E_{\perp}$, and the magnitude of the tangential component $|\mathbf{E}_{\parallel}|$ for one exemplary subject. The electric field was normalized to allow comparability between the different experimental conditions. The white circle shows the M1 hand knob area.

more detailed description of this procedure is given in Section 1.2 of the *Supplementary Material*.

Because the electric field scales the I/O curves linearly eq. (3) can be reformulated in terms of stimulator intensity which allows a highly efficient implementation. A detailed mathematical description is also given in Section 1.2 of the *Supplementary Material*. The above described shift approach for the computation of the congruence factor is especially useful, if the experimentally determined I/O curves capture only a linear or exponential part of the relationship between the electric field and MEP amplitude (see above). If, however, each E-MEP curve can be represented as an analytical sigmoidal function, parameterized by its turning point $x_{0,i}$, the shifts τ_i are directly given by $\tau_i = x_{0,i}E_i(\boldsymbol{r})$. This approach is advantageous in terms of computational cost and is preferred in the current study if all I/O curves are modelled by sigmoidal functions.

As the standard Freesurfer average template (FsAverage) suffers from several malformed elements at the primary motor cortex, each roughly 20-fold the size of the average elements, we created a group-based average with Freesurfer. In this iterative procedure a randomly chosen subject was used as the initial template and all other subjects were registered to this. In the second step, the template was updated based on these registrations. The third step comprised the registration of all subjects to this updated template. The second and third steps were then repeated to improve the template.

2.4. Uncertainty and sensitivity analysis

The congruence factor is influenced by several parameters. For example, previous studies have shown that, because of their large uncertainties, the electrical ohmic conductivity of brain tissues have a strong influence on the magnitude of the electric field (Weise et al., 2015; Codecasa et al., 2016; Saturnino et al., 2019). Furthermore, the estimated parameters of the fitted MEP curves are also uncertain due to measurement uncertainties (Fig. 3b, grey interval). Therefore, uncertainty and sensitivity analyses are important to investigate the stability of the results and identify the parameters and their combinations with the largest impact on the results.

Since the problem is computationally complex and features a large number of parameters $\boldsymbol{p}$, an efficient approach is necessary to conduct the analyses. Here, we applied the generalized polynomial chaos (gPC) method (Ghanem et al., 2016). Its mathematical background is described in detail in Section 1.4 of the *Supplemental Material*. In short, the gPC is based on the construction of a polynomial surrogate of the congruence factor depending on the uncertain model parameters and their associated probability density functions.

Since the electric field depends on the electrical conductivity $[\sigma]$ of the brain tissues, the congruence factor will be influenced by varying conductivity as well. The conductivity of GM, WM, and CSF were modelled as beta distributed random variables. The impact of errors of conductivity values in other tissues (e.g., skull and scalp) on the electric field has been shown to be negligible in previous studies (Codecasa et al., 2016; Saturnino et al., 2019). However, extending previous studies, the impact of the level of conductivity anisotropy was included in our analysis. The conductivity tensor $[\sigma]$ for each voxel was derived from the diffusion tensor using the volume normalize approach (Güllmar et al., 2010). This tensor can be visualized as ellipsoid (see Fig. S3). A spherical ellipsoid represents isotropic conductivity with equal conductivity in each direction, while a cigar shaped tensor indicates that the conductivity is much larger in one direction. We implemented an anisotropy scaling factor α that transforms the diffusion tensor from the isotropic case ($\alpha = 0$) via the original tensor obtained from DTI ($\alpha = 0.5$) to a very anisotropic case ($\alpha = 1$). Although, in principle, α could be different in each voxel, this would render the resulting problem intractable. Instead, we assume that α is the same for all voxels. This reflects systematic errors and uncertainties in the transformation between the diffusion tensor, which

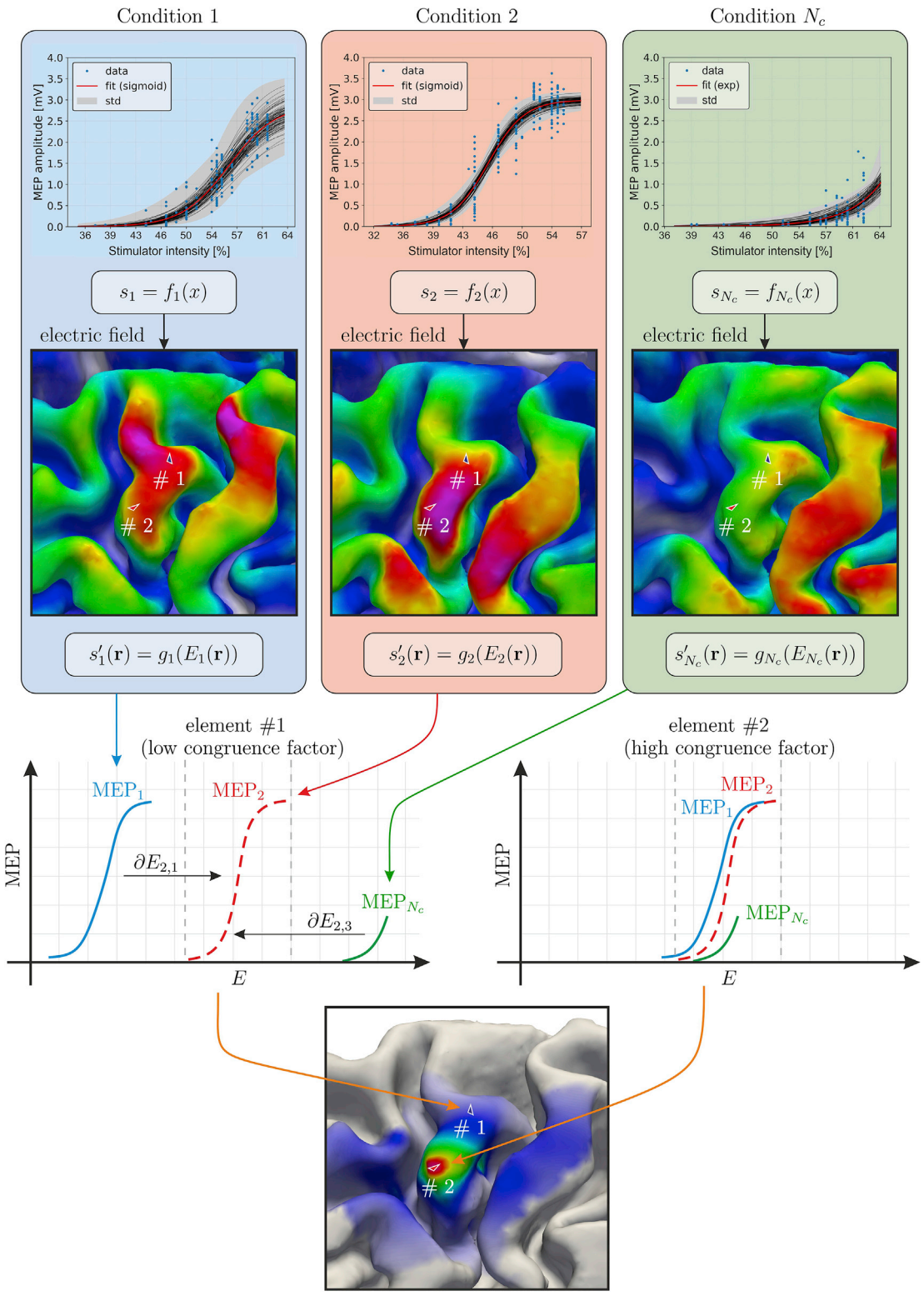

Fig. 6. Principled approach to determine the functionally relevant site of activation by TMS. The *congruence factor* is based on the assumption that the electric field, which is causal to the observed behavioral effect, corresponds for the experimental conditions. The measured I/O curves are transformed to element wise E-MEP curves using electromagnetic field modeling (see text). The congruence factor between the E-MEP curves inversely depends on the amount of transformation (shift) necessary to obtain maximum overlap between the E-MEP curves in each element.

depends on the mobility of water molecules, and the conductivity tensor, which represents the mobility of charges. A detailed mathematical description of the parametrization of the fractional anisotropy is given in *Supplemental Material:* Section 1.3.

In addition to the conductivity and anisotropy uncertainties, the turning points $x_{0,i}$ from the sigmoidal I/O curves were included in the uncertainty analysis. Their uncertainties were derived from the confidence intervals of the curve fits (see Fig. 3b). The stochastic properties of all investigated parameters are summarized in Table 1. The model of the congruence factor used in the gPC-based uncertainty and sensitivity

analyses is described in detail in *Supplemental Material:* Section 1.5.

After deriving the polynomial surrogate using the gPC, the spatial distribution of the expectation $\mu(\boldsymbol{r})$ and the variance $\nu(\boldsymbol{r})$ of the congruence factors $c(\boldsymbol{r})$ can be calculated. We further analyzed the relative standard deviation $RSD = \sqrt{\nu(\boldsymbol{r})}/\mu(\boldsymbol{r})$ to identify possible parameter ranges where the congruence factor is primarily influenced. Finally, in the sensitivity analysis, the variance was decomposed into its origins by a Sobol decomposition. The Sobol indices $S_i(\boldsymbol{r})$ represent portions of the total variance $\nu(\boldsymbol{r})$, which are due to individual parameters p_i or a combination thereof, e.g. the conductivity of GM or the combination between different measurement parameters (Sobol, 2001; Sudret, 2008).

2.5. Validation

To validate the estimated sites of effective stimulation, we first determined the corresponding optimal coil position and orientation that maximizes the electric field magnitude in the previously determined congruence factor hotspot for each of the three subjects in Experiment II. This was done by using an exhaustive search optimization procedure. First, we projected the individual congruence factor hotspot to the skin surface. Thereafter, we defined a dense circular grid (radius 20 mm, spacing 1.5 mm) of coil positions and orientations around that position, as shown in Fig. S5. The orientations were defined in the interval from −90° to 90° around the PA-45 orientation in steps of 15°. This was motivated by the fact that the magnitude does not uniquely reflect the electric field vector. At least, there are always two vectors with opposite signs originating from opposite coil orientations (or current directions) that generate the same magnitude. Therefore, for the optimization we only considered coil orientations with a positive component into the PA-45 direction. Finally, the search grid comprised about 4500 different coil configurations. On this grid, we searched for the coil position and orientation that produces the maximum electric field magnitude at the cortical target. We implemented this optimization routine in SimNIBS v3.1 (https://github.com/simnibs).

If the determined congruence factor hotspot is indeed the origin of the observed effects, then the MT should be lowest for the optimized coil position/orientation. We therefore experimentally compared the MTs obtained for these optimal coil configurations to those obtained for other adjacent coil configurations. For MT determination, single biphasic pulses with 5 s ISI were applied.

Table 1
Limits and shape parameters of the model parameters for subject Sub01. The parameters p and q denote the shape parameters of the beta distributions and x_0 are the turning points of the sigmoidal I/O curves.

Parameter	Description	Min	Max	p/q	Reference/source
σ_{WM}	White matter conductivity in S/m	0.1	0.4	3/3	Li et al. (1968) Nicholson (1965) Akhtari et al. (2010)
σ_{GM}	Grey matter conductivity in S/m	0.1	0.6	3/3	Li et al. (1968) Ranck (1963) Logothetis et al. (2007) Yedlin et al. (1974)
σ_{CSF}	Cerebrospinal fluid conductivity in S/m	1.2	1.8	3/3	Gabriel et al. (2009) Baumann et al. (1997)
α	Anisotropy scaling	0.4	0.6	3/3	Tuch et al. (2001)
$x_{0,S(90°)}$*	MEP curve turning point in A/µs	145.9	185.9	4/4	experiment
$x_{0,S(135°)}$*	"	150.0	190.0	4/4	"
$x_{0,I(45°)}$	"	80.7	87.9	4/4	"
$x_{0,I(135°)}$	"	125.7	145.7	4/4	"
$x_{0,P(0°)}$	"	124.2	133.3	4/4	"
$x_{0,M1(90°)}$	"	86.0	98.7	4/4	"

Note: These parameters were considered in the uncertainty and sensitivity analysis to determine the site of activation by means of the congruence factor. The asterisk marks conditions, where only the lower tail of the I/O curve could be determined. These curves are subject to a higher measurement uncertainty.

3. Results

In the following sections, we present the results from Experiment I (15 subjects and 6 experimental conditions, Section 3.1) and Experiment II (3 subjects and 20 experimental conditions, Section 3.2). The latter includes a permutation analysis to determine the minimum number of TMS conditions, that is coil positions and orientations required to identify the location of the cortical representation of the MEPs reliably. Then, we validated the predicted cortical sites of activation for the subjects in Experiment II (Section 3.3). Finally, the results of the uncertainty and sensitivity analyses of the congruence factor are presented for one exemplary subject (Section 3.4). The most influential parameters of the numerical model and experimental data are identified in the ensuing sensitivity analysis.

3.1. Experiment I (15 subjects, 6 experimental conditions)

An average of 981.6 (SD = 173.1) single pulses were applied per subject (163.6 (SD = 49.4) per coil position/orientation). Fig. 7 shows the congruence factors of the group average and the 15 individual subjects. The electric field distributions of all conditions were determined for each subject and combined with the fitted MEP curves using the *optimal curve shift approach* because not all MEP curves could be fitted to sigmoidal functions. In 6/15 subjects (marked with an asterisk, *), no I/O curve could be determined for the posterior coil position $P_{0°}$. Hence, the congruence factor was determined using only 5 of the 6 conditions. The congruence factor was calculated for the overall magnitude ($|\mathbf{E}|$), as well as the normal ($E_\perp = \mathbf{E}\cdot\mathbf{n}$) and the magnitude of the tangential ($|\mathbf{E}_{||}|$) component of the induced electric field. The overall magnitude and the magnitude of the tangential component reached substantially higher congruence factors and smoother spatial distributions than the normal component $c(E_\perp)$. In general, a clear hotspot for $c(|\mathbf{E}|)$ and $c(|\mathbf{E}_{||}|)$ could be identified in the hand knob area of M1 on the gyral crown of the average template. Considering the individual congruence factor maps we found clear and unique hotspots on the gyral crowns in the hand knob area in 7/15 subjects (Sub01-Sub07, highlighted in Fig. 7 with a green background). In 4/15 subjects (Sub08-Sub11, Fig. 7, yellow background), we observed a second hotspot in the somatosensory cortex. In 4/15 subjects (Sub12-Sub15, Fig. 7, orange background), we could only identify a dominant hotspot in the somatosensory cortex. We reasoned that this was due to array ambiguities, i.e., spurious overlaps, of the realized electric fields and the missing I/O curve of condition $P_{0°}$, in 2/4 and 3/4 subjects of the two groups, respectively. Note that maximum values of the congruence factors substantially differ across subjects. This is because small differences in near zero variances among I/O curves may result in large differences in their inverse, that is, the associated congruence factors.

We expected that additional experimental conditions, i.e., more coil positions and orientations, would improve the results of the congruence factor towards more plausible hotspot locations in the M1 hand knob area. This hypothesis was investigated in Experiment II by increasing the number of coil positions and orientations from 6 (respectively 5) to 20 (see Fig. 2b). We selected one subject from each of the three result groups described above (Sub01, Sub08, and Sub12) for this experiment.

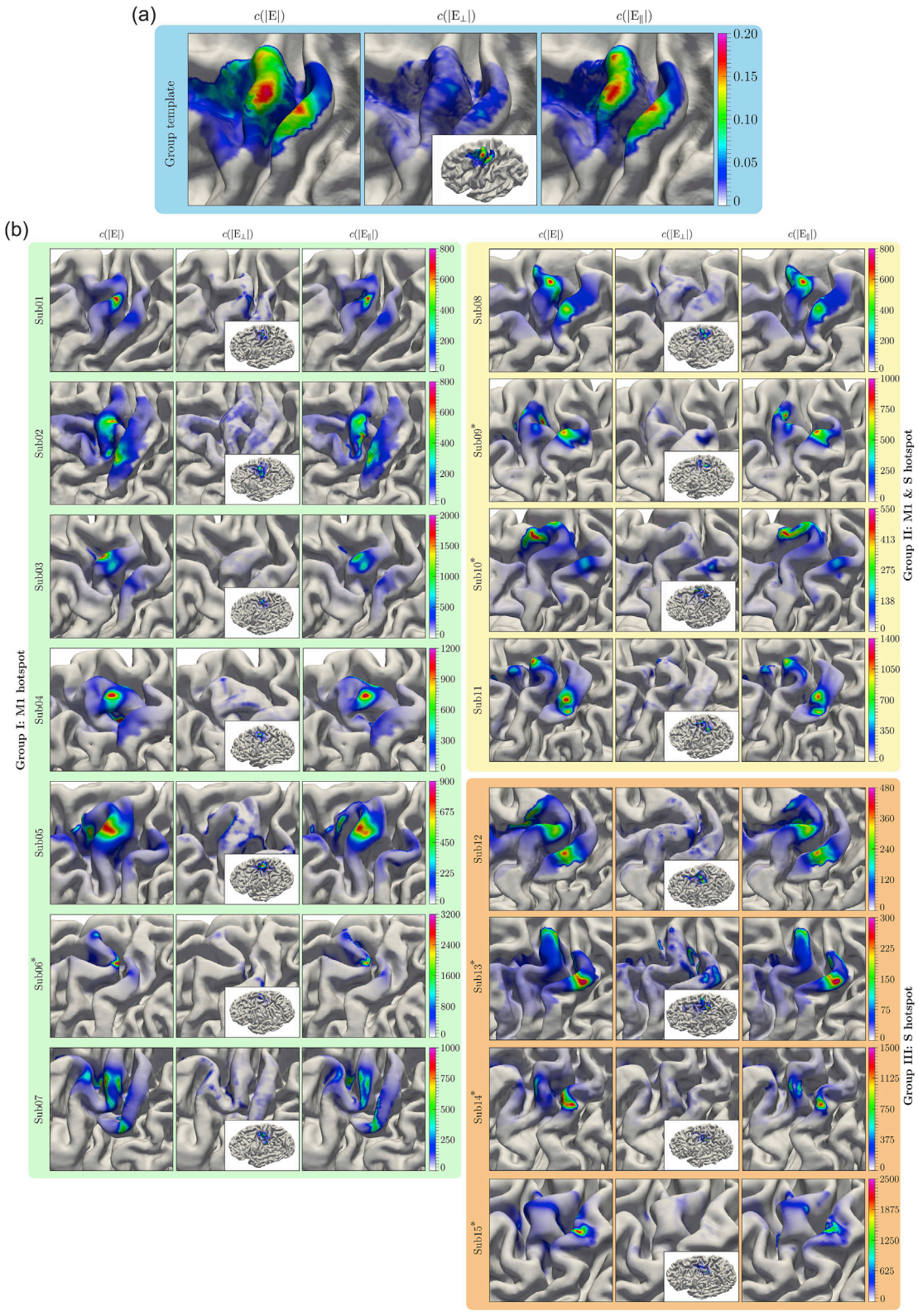

Fig. 7. (a) Average and (b) individual congruence factor maps of all 15 subjects including six experimental conditions (Experiment I). The congruence factors were calculated for the overall magnitude, the normal component, and the magnitude of the tangential component of the electric field using the optimal curve shift approach. 7/15 subjects show unique hotspots in M1 (highlighted in green); 4/15 subjects show hotspots in M1 and the somatosensory cortex (highlighted in yellow) and 4/15 subjects show hotspots in the somatosensory cortex only (highlighted in orange); the asterisks (*) mark subjects where no evaluable MEPs could be determined for the posterior coil position P_{0°. In these cases, the congruence factor was determined using only five conditions; all results were normalized, mapped and superimposed on the group average template shown on the top (highlighted in blue).

3.2. Experiment II (3 subjects, 20 experimental conditions)

This experiment was conducted with an extended set of coil positions and orientations (Fig. 2b). For each subject, 20 electric field distributions were calculated and combined with the obtained MEP curves to determine the congruence factor maps. An average of 1831.3 ($SD = 300.52$) single pulses were applied per subject (85.84 ($SD = 17.19$) per condition). In this experiment, all I/O curves could be fitted to sigmoidal functions, which avoids the computationally expensive optimization step from eq. (3) by directly using the variance of the turning points.

Applying 2000 single pulses with a comparatively short 4 s ISI alone takes about 2.5 h; additional time for subject preparation, changing the coil position and rotation, potential pauses due to coil heating, rest periods for the subject, etc. may lead to experiment durations of 5 h or more. Since this would not be feasible in everyday (clinical) applications, we investigated how the congruence factor convergences depending on the number of experimental conditions. This enabled us to determine an optimal number and selection of coil positions/orientations to reduce the experimental effort. Consequently, a permutation study was performed for each subject by determining the congruence factor for all combinations of $k = 2 \ldots 20$ available experimental conditions. The total number of considered conditions was $\sum_{k=2}^{20} \binom{20}{k} = 1,048,555$. We quantified the focality of each congruence factor map by determining the area with $c > 30$. This threshold was chosen based on the permutation results to allow comparability between the combinations and subjects. The smaller this area, the more concentrated the map is. That is, the more uniquely the relationship between electric field and MEP could be determined.

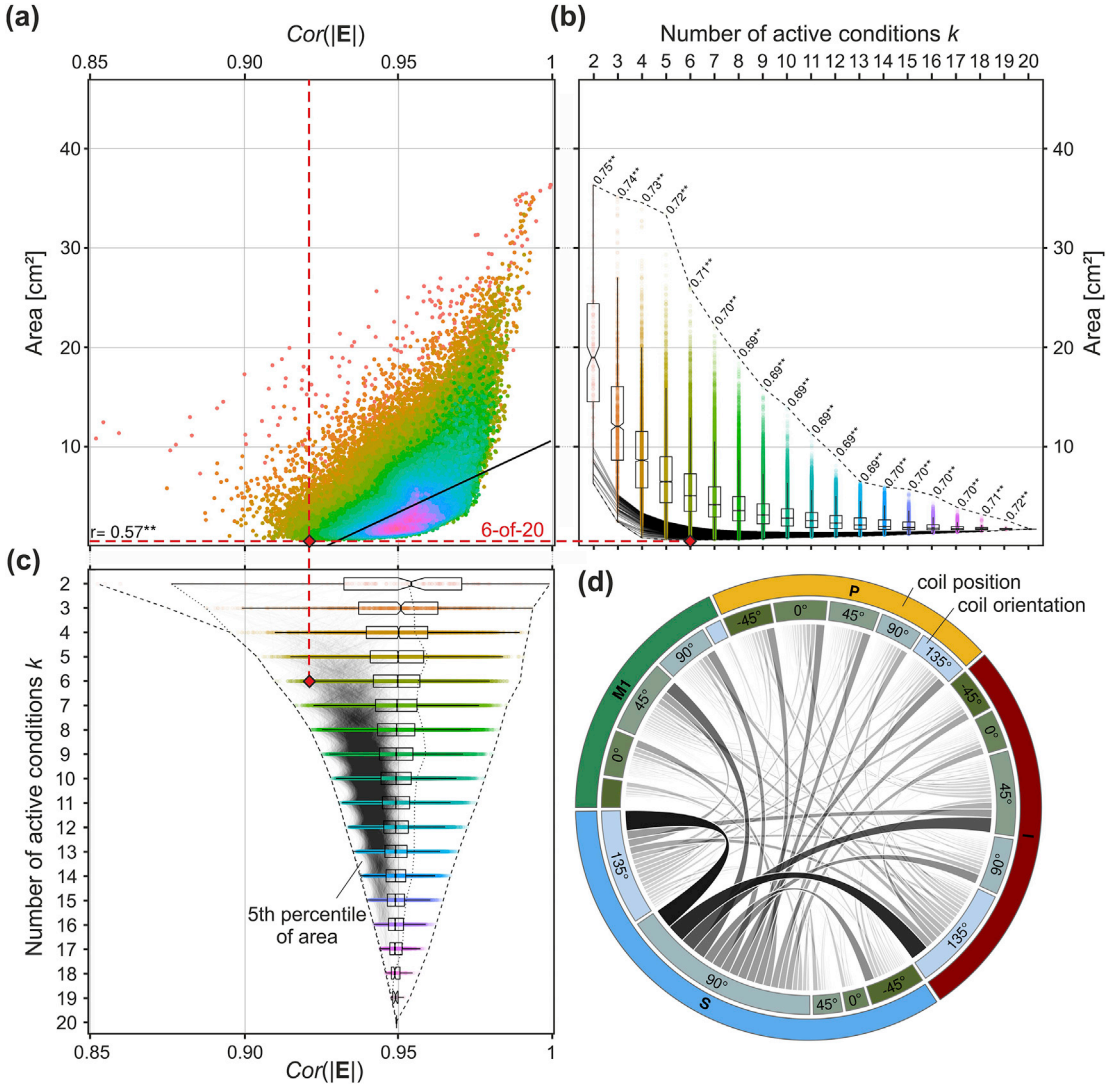

Fig. 8. Permutation analysis interrelating the cross-correlation of the electric fields from the different experimental conditions of Experiment II for subject Sub01 with the corresponding hotspot area. The hotspot area was defined as the region where $c > 30$. For each case k, the congruence factor was determined $(20\ k\ )$ times. (a) Relationship between the cross-correlation of the electric field magnitude and the resulting hotspot area size. Colors: active conditions k. The correlation coefficient between the hotspot size and the cross-correlation of the electric fields over all k (black line) is $r = 0.57$ $(p \ll 0.001)$. (b) Boxplot of the hotspot area of the congruence factor depending on the number of active conditions k. Box areas indicate the 25%–75% quantiles with notch at median. Correlation coefficients between the hotspot size and the cross-correlation of the electric fields for each k are given. ** depict $p < 0.01$ (after Bonferroni correction). Grey lines: 5th percentile of the best condition combinations for each k. Dashed lines: absolute range. The variation of the hotspot area size decreases with increasing k. (c) Relationship between the cross-correlation coefficient of the electric fields and the number of active conditions k. Box areas indicate the 25%–75% quantiles with notch at median. Grey lines: 5th percentile of the best condition combinations for each k. Dashed lines: absolute range. The dashed red lines highlight the case of the 6 coil positions and orientations, where the congruence factor map was most focal. Its cross-correlation coefficient is with 0.921 lower than the first quartile of possible solutions. (d) Chord graph highlighting the interaction and relative contribution between different coil positions (outer circle) and coil orientations (inner circle) from the 5th percentile of best condition combinations over all k resulting in small hotspot areas (highlighted with black lines in (b)).

The results of the permutation study are shown in Fig. 8 for one exemplary subject (Sub01). The results for the remaining subjects were similar (see Figs. S7–S9, respectively). We expected that a lower cross-correlation across the condition-wise electric fields would allow for a higher discriminative power in the determination of the stimulation site. This was confirmed by the analysis in Fig. 8a, showing a correlation of $r = 0.57$ ($p \ll .001$) between the size of the hotspot area and the cross-correlation of the electric fields over all k. As obvious from the individual number of conditions k, the correlation between the resulting hotspot area and the cross-correlation of the electric fields was stronger for low k (Fig. 8b, correlation coefficients). The median of the hotspot area converges when increasing the number of active conditions. Moreover, the spread of the area decreases by adding more information to the congruence factor calculation. Importantly, the smallest areas (lower dashed line in Fig. 8b) indicate that some condition combinations for $k \geq 5$ result in similar or even smaller areas than for $k = 20$. This suggests that the cortical site of activation can be determined with relatively few measurements by selecting optimal coil positions and orientations.

The relationship between the cross-correlation of the electric fields and the number of active conditions k is shown in Fig. 8c. Cases resulting in the smallest 5th percentile of the hotspot area are shown as thin lines in the shaded area, corresponding to those shown in Fig. 8b. As expected, these cases are concentrated in regions of low cross-correlation.

The data were further analyzed to identify which combinations of experimental conditions were especially informative and produce very focal hotspots (Fig. 8d). This analysis was performed for $k = 6$. The appearance of each condition and its co-occurrence with other conditions was accumulated across all condition combinations, which are part of the smallest 5th percentile of the hotspot area (grey shaded area in Fig. 8b). We found that the co-occurrence was not random and combinations surrounding M1, i.e., inferior, superior, and posterior, appeared more often than coil positions directly over M1. The corresponding coil orientations differ considerably and connections between $S_{90°}$, $S_{135°}$, $I_{45°}$, and $I_{135°}$ stand out. Moreover, it can be observed that posterior conditions occurred frequently in combination with $S_{90°}$, which further confirms the need for highly varying electric field distributions. This behavior was even more pronounced for subjects Sub08 and Sub12 (see Figs. S7–S9).

Next, the condition combination that led to the smallest hotspot ($k = 6$) is described in more detail and compared to Experiment I and the full

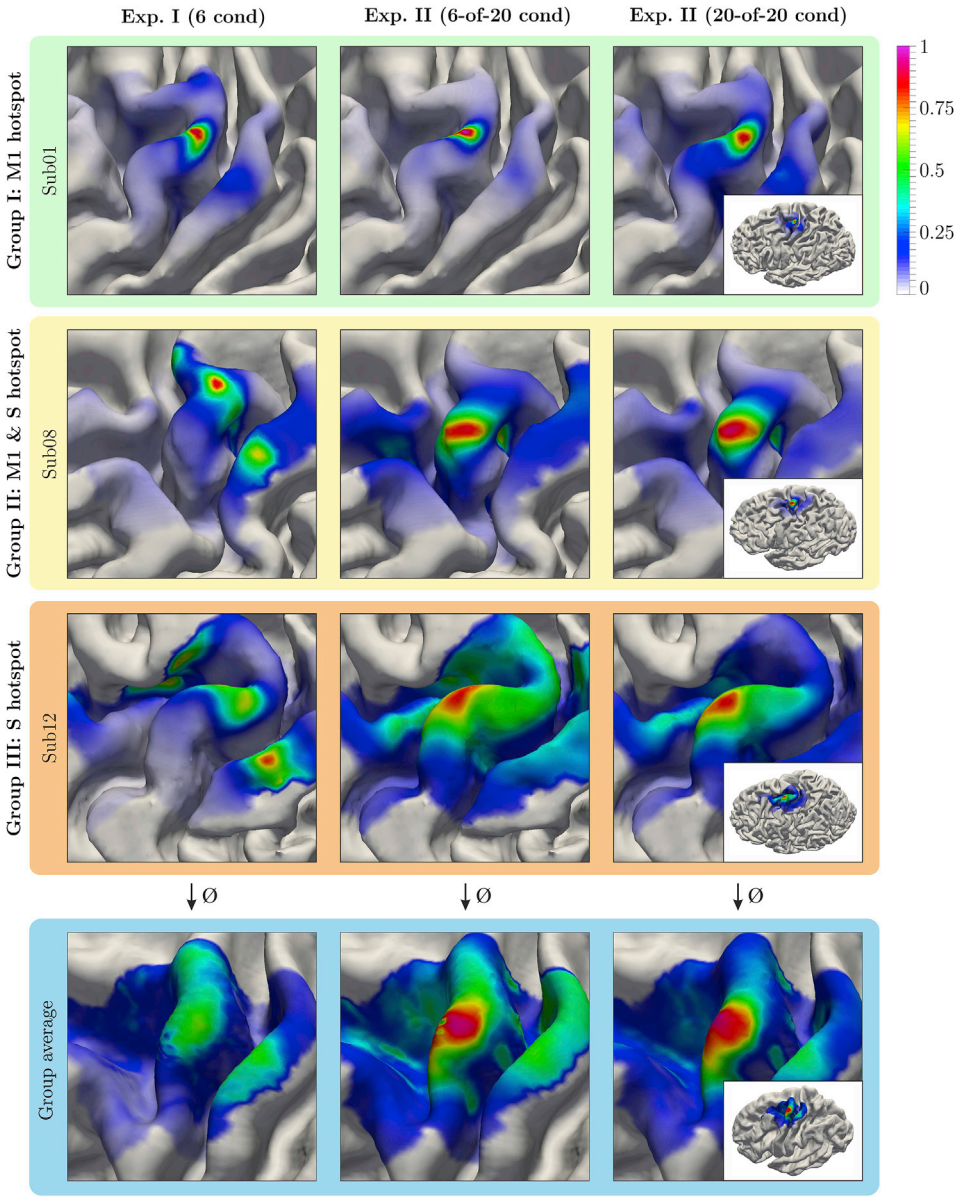

Fig. 9. Normalized congruence factor maps of 3 subjects. The first column shows the results of Experiment I with 6 experimental conditions; the middle row depicts the 6-of-20 condition combination with the smallest hotspot area from Experiment II; the right column shows the congruence factor maps when all 20 experimental conditions of study II are included in the analysis. The subjects were chosen to include on participant from each result group in study I (M1 only, M1 and somatosensory cortex, and somatosensory cortex only, see Fig. 7).

$k = 20$ result. Applying the method for 6 different coil conditions and orientations is also feasible, as the total experiment duration should not exceed 1 h.

The results are shown in Fig. 9 for each subject. The congruence factor maps were normalized with respect to their individual maxima to allow comparability. For subject Sub01, we already found a unique hotspot in the M1 hand knob area in Experiment I. The results of Experiment II show that this pattern is reproducible and even more focused (as the deflection on the somatosensory cortex is weaker) for the best 6 condition combination (6-of-20). Hence, for this subject, the coil positions of Experiment I were already sufficient to determine the site of activation in a plausible manner. The second subject belonged to the group with hotspots in both M1 and the somatosensory cortex (Experiment I). In Experiment II, a single hotspot was found, limited to the M1 region, with the deflection in the somatosensory cortex disappearing. The M1 hotspot was also slightly shifted inferiorly. The third subject belonged to the group that showed a hotspot only in the somatosensory cortex in Experiment I. In Experiment II, however, the hotspot moved to M1. This supports our assumption of insufficient information content concerning the combination of electric field profiles and measured MEP amplitude curves, likely due to a limited classification ability of the electric fields. As indicated by the convergence results of the permutation study (Fig. 8a), adding the remaining conditions of Experiment II (20-of-20 case) does not yield any improvement for any of the three subject groups.

For subject Sub01 (first row in Fig. 9), the cross-correlation of the electric field distributions in the ROI was 0.951 for Experiment I, and 0.921 for Experiment II. For subject Sub08 (second row in Fig. 9), the cross-correlation was 0.953 and 0.925 for Experiment I and II, respectively. We found that the use of less correlating electric field distributions increased the quality of the reconstruction. Finally, for subject Sub12 (third row in Fig. 9) the cross-correlations were nearly the same with 0.951 and 0.953 from Experiment I to II, respectively. However, the improvement of the results indicates that the selected coil positions and orientations in Experiment II were more suitable to determine the congruence factor, resulting in a higher distinguishability between the cortical positions. We wish to emphasize that this property is only partly reflected by the cross-correlation coefficient. A definition of a more sophisticated ambiguity measure to determine an optimal set of coil positions and orientations will be the subject of a future study.

3.3. Validation

After determining the optimal coil positions and orientations for the subjects in Experiment II, we validated the predicted cortical sites of activation, as described in Section 2.5.

Due to health issues unrelated to this study, subject Sub12 from group III (see Fig. 9) was not able to participate in the validation study. We replaced this subject with subject Sub15 from group III and repeated Experiment II. It turned out that using the predefined 20 conditions did not yield a single pronounced congruence factor hotspot for this subject. To increase electric field variance, we added further conditions at different positions, orientations, and tilting angles of the TMS coil (see Fig. S6). We additionally determined the corresponding best 6-of-30 condition combination yielding very similar results compared to the full 30 condition analysis. The results are shown in Fig. 10. Notably, all computationally determined optimal coil orientations were similar to the commonly used 45° angle towards the *fissura longitudinalis* (Brasil et al., 1992; Mills et al., 1992). Note that by using the field magnitude we are not able to distinguish between opposite coil orientations. Therefore, our optimization space was restricted to ±90° around the PA-45 direction.

In an additional validation experiment, we determined the MTs for the determined optimal coil configuration as well as for a number of adjacent positions and orientations. Based on our observations regarding the sensitivity of the MT towards coil position and orientation we chose spacings of about 7 … 10 mm in position and 30° for orientation between the tested configurations (see Fig. 11).

As shown in Fig. 11, the MTs were always lowest for the predicted optimal coil configuration. This confirms the validity of the calculated congruence factor hotspots.

3.4. Uncertainty and sensitivity analysis

We analyzed the congruence factor in terms of uncertainty and sensitivity towards the electrical conductivity in the 6-of-20 case for the following parameters: the brain tissues, CSF, fractional anisotropy, and measurement inaccuracies informed from I/O curve fit deviations, for all subjects of Experiment II. The results from subject Sub01 are shown in Fig. 12. The results of subject Sub08, Sub12, and Sub15 are shown in Figs. S10–S12. The uncertainties of the model parameters are listed in Table 1 and Table S1-S3. The spatial distributions of the mean, the relative standard deviation (*RSD*), and the variance (*VAR*) of the congruence factor are shown in Fig. 12a. The mean distribution shows a hotspot, which extends from the gyral crown of M1 to the upper parts of the anterior sulcal wall. *RSD* and *VAR* indicate that the congruence factor could be determined with a greater certainty ($RSD \approx 12\%$) on the gyral crown than on the anterior sulcal wall ($RSD \approx 40\%$).

To identify the most influential model parameters, we decomposed *VAR* into its origins with a Sobol decomposition. The spatial distributions of the absolute first order Sobol indices on the cortex are shown in Fig. 12b. The Sobol coefficient maps of the MEP curve parameters are accumulated on one Sobol index termed Sobol (EXP). The average first order and highest second order Sobol indices are depicted in Fig. 12c for all subjects of Experiment II. The average was computed over the elements in the ROI. The parameters that contributed most to the uncertainty of the congruence factor were the electrical conductivity of GM (σ_{GM}) and WM (σ_{WM}) as well as the uncertainty of the measured MEP curves (EXP) for all subjects. Their relative contribution to the total variance, shown in Fig. 12d and in Figs. S10d–S12d, was subject specific and depended on the accuracy of the measured MEP curves as well as the brain anatomy influencing the electric field distribution. The uncertainty

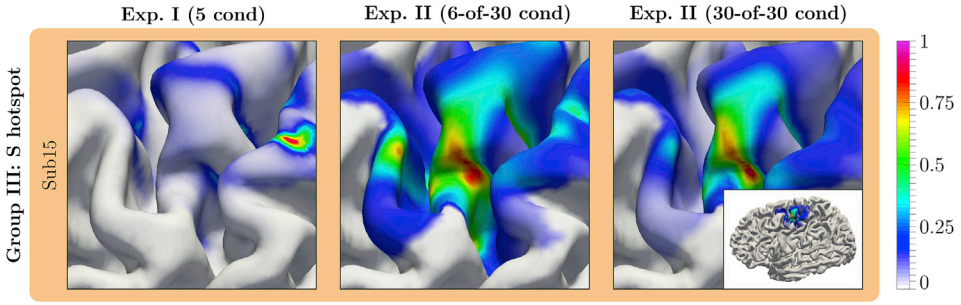

Fig. 10. Normalized congruence factor maps of subject Sub15, replacing subject Sub12 from subject group III for the validation. The first column shows the results of Experiment I with 5 experimental conditions; the middle row depicts the 6-of-30 condition combination with the smallest hotspot area from Experiment II; the right column shows the congruence factor map when all 30 experimental conditions of study II are taken into account.

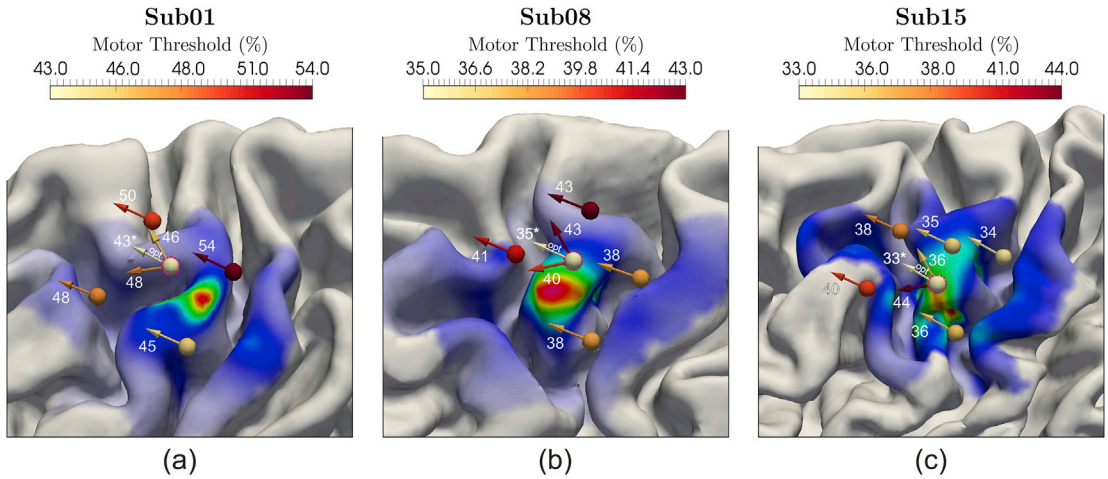

Fig. 11. Coil positions and orientations used to validate the identified cortical site of activation. The optimal coil position is marked with a dashed purple circle and its corresponding optimal orientation is indicated by "opt". Numbers represent the rMTs: the lowest stimulator intensity, that elicited 5 of 10 consecutive MEPs with amplitudes >50 μV. Lowest rMTs at the optimal coil positions and orientations are marked with an asterisk.

of the congruence factor hotspot in the anterior sulcal wall predominantly originated from the uncertainty of σ_{GM} and the measurement uncertainties indicated that this hotspot was likely to be spurious.

4. Discussion

In the present study, we introduce a novel approach to localize the functional relevant cortical site for a given physiological variable with transcranial magnetic stimulation (TMS). We link numerical modeling of the induced electric field with measurements of peripheral physiological responses to demonstrate considerably improved localization. With this approach, we were able to localize the cortical area most likely responsible for the observed motor output caused by single TMS pulses applied over the primary motor cortex. Our main finding is that sharply bounded neural structures located in the gyral crowns, and extending to the upper parts of the sulcal wall of the motor hand area, represent the most likely origin of the motor evoked potentials. We identified the overall magnitude and the magnitude of the tangential component of the electric field as the relevant quantities for modulating the observed effect.

Our results suggest that unique results can be obtained with relatively few trials or measurements per subject. Based on our findings, we derive principles for the selection of the respective coil positions that may help to improve localization of TMS effects in future applications, both at the single subject and group level. Our first experiment combined two different coil positions with three coil rotations each, yielding 6 conditions. The induced electric fields were computed with finite element models (FEM), allowing for the assessment of element-wise E-MEP relations. We identified three groups with a hotspot at either primary motor cortex only, the somatosensory cortex only, or both. One subject from each group was included in the extended second experiment with 4 sites and 5 rotations, yielding 20 conditions. For the subject from the M1-group, the hotspot was replicated at the same spot. For the subjects from the other two groups, the original results could be significantly improved with single hotspots at the gyral crowns and the upper parts of the sulcal walls of the motor hand area observed in each case. The final validation study in three subjects confirmed that optimizing the TMS coil position and orientation, such that it maximized the electric field at the predicted cortical target, indeed resulted in a minimization of the motor thresholds (MTs).

The congruence factor employed in our study quantifies the correlation between the measured physiological variable (here, the MEP) and the induced electric field profiles. Note that the proposed approach does not depend on the involved function types to describe the I/O behavior. This provides a high level of flexibility and makes the method easy to adapt to other applications and domains. We conclude that our approach significantly improves the localization of effectively stimulated areas during TMS and may increase the power and reliability of the resulting effects in future TMS studies at the individual level.

4.1. Linking our results to prior studies relating TMS electric fields to MEPs

Based on our results, we argue that voxels with maximum congruence factors are good candidates for functionally relevant cortical areas. Importantly, in all subjects, we found that higher variability between electric fields sharpened the localization results. Sets of experimental conditions that selectively varied coil position or coil orientation did not contain sufficient information to uniquely determine the location of cortical representation. Moreover, placing the TMS coil directly over M1 with a 45° orientation, though yielding the strongest effect, was by far not the most informative condition using our method. This can be explained by the relatively wide distribution of the electric field in the motor area, resulting in low discriminative power for such a coil (standard figure-of-eight). These observations may also provide an explanation for the spurious second hotspot in the somatosensory cortex observed by Bungert et al. (2017), when applying TMS pulses selectively over M1, and Laakso et al. (2018), when orienting the TMS coil 45° towards the *fissura longitudinalis* (Brasil et al., 1992; Mills et al., 1992). Notably, we observed similar effects in Experiment I, when only 5 or 6 non-optimal experimental conditions were considered (subject group II and III, Fig. 7). Reducing the correlation of the electric fields across the tested positions and orientations considerably enhanced the localization capabilities of our method in all subjects (Experiment II). This observation was further supported by a permutation analysis showing that higher variability between the spatial patterns of the electric fields, using specific combinations of coil positions and orientations, considerably increased the accuracy of the localization results.

Interestingly, previous studies that selectively incorporated the 45° coil orientation (corresponding to coil orientations $M1_{45°}$, $P_{45°}$, $S_{45°}$ in this study) towards the *fissura longitudinalis* (Laakso et al., 2018; Krieg et al., 2013; Salinas et al., 2011) appear to support sulcal wall activation by the normal component of the electric field. In contrast, studies that involved different coil orientations (Bungert et al., 2017) highlight $|\mathbf{E}|$ and gyral crowns (corresponding to coil orientations $M1_{-135°}$ $M1_{-90°}$, $M1_{-45°}$, $M1_{0°}$, $M1_{45°}$ in this study). Recent results from direct electric stimulation (Aonuma et al., 2018) support the latter, which contrasts with the conclusions drawn from studies using only imaging techniques (Fox et al., 2004; Krieg et al., 2013). However, both methods have the major disadvantage that their resolution is not sufficient to identify the

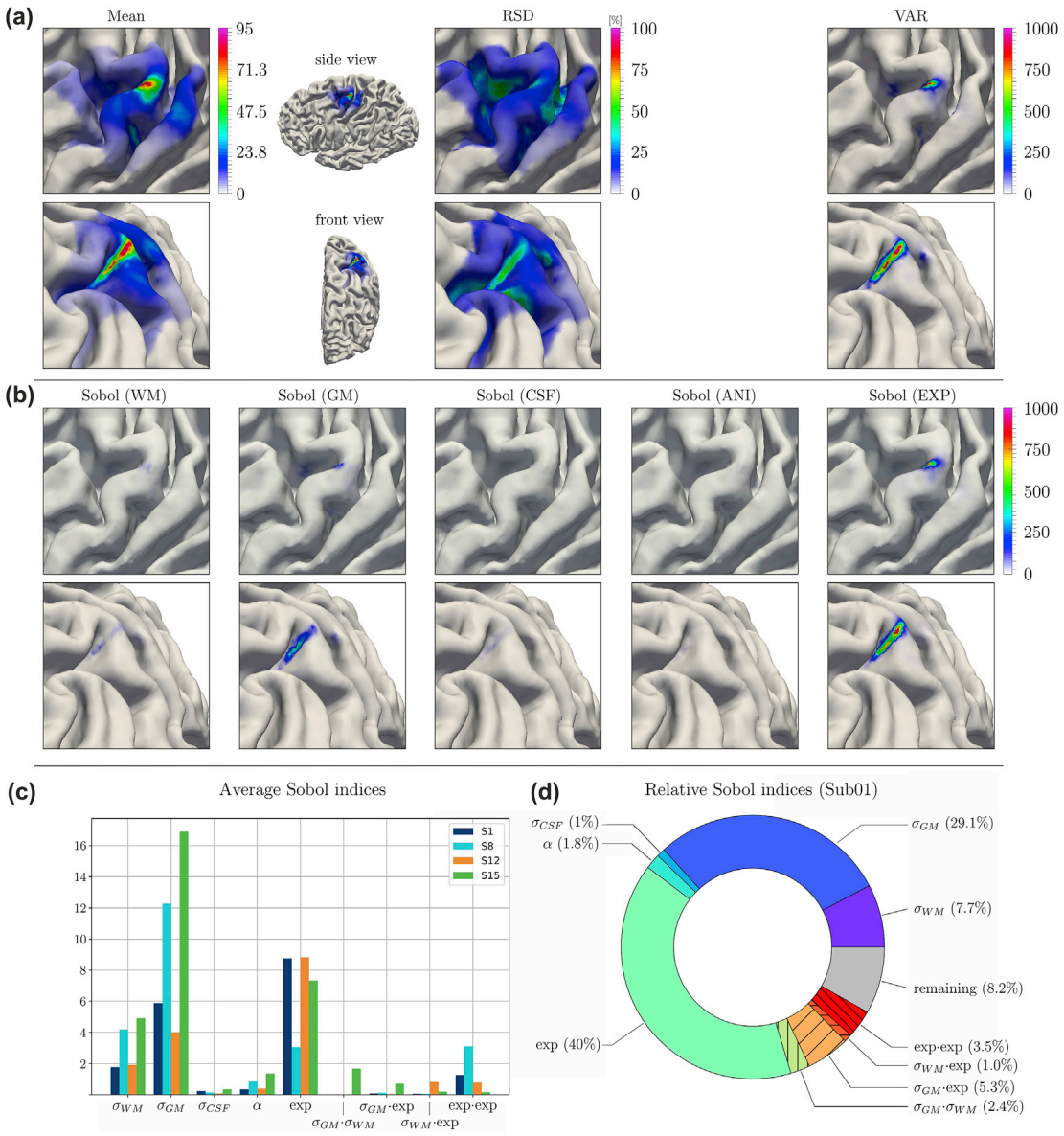

Fig. 12. Uncertainty and sensitivity analysis of the congruence factor determined for subject Sub01 in the 6-of-20 analysis of Experiment II. (a) Expected value (*Mean*), relative standard deviation (*RSD*), and variance (*VAR*) of the congruence factor. (b) Spatial distributions of the absolute first order Sobol indices. The normalization with respect to the total variance was avoided to strengthen the focus on regions of high variance (see Eq. (12) in the *Supplementary Material* on how the Sobol indices are computed). The Sobol index maps of the individual MEP parameters resulting from uncertainties in the experimental data are summarized into one Sobol index map *Sobol (EXP)*. (c) Average first order Sobol indices for subjects Sub01 (shown here), Sub08, and Sub12. The average was computed over the elements in the ROI (d) Relative first order Sobol indices averaged over the ROI. For (a) and (b) two different perspectives are shown (top and bottoms rows), to improve visibility of the effects.

part of the cortex that is effectively stimulated. By changing both, i.e., coil position and orientation, we observed low congruence factors for the normal component of the electric field at the anterior wall of the central sulcus. Since low congruence factors highlight areas where the behavioral effect does *not* correlate with changes in the local electric field, our results indicate that the previously proposed stimulation mechanism by the normal component (Laakso et al., 2018; Fox et al., 2004; Krieg et al., 2013) cannot explain the observed effects for all experimental conditions. In contrast, we found that the magnitude of the tangential component (and therefore also the overall magnitude) of the field showed reasonable congruence factor maps. This finding suggests that the gyral crowns and upper parts of the sulcal wall are the most likely origin of the motor evoked potentials.

Two prior studies have superimposed the calculated electric fields, either in an additive or multiplicative fashion, to localize the cortical position targeted by TMS (Opitz et al., 2013; Aonuma et al., 2018). Opitz et al., 2013 weighted the computed electric fields with the strengths of the observed effects and overlaid the fields in an additive fashion. In contrast, Aonuma et al. (2018) superimposed the fields in a multiplicative fashion after selecting the experimental conditions for which the observable effect exceeded a particular threshold. The latter may be disadvantageous since it uses only a small portion of the information contained in the measurement. Both methods approximate a covariance between the field strength and the MEP amplitude. However, this covariance does not only depend on the correlative relationship between the two, but also on the general magnitude of the field across conditions. This leads to a strong bias towards voxels which generally receive higher field strengths (i.e., on gyral crowns) for both approaches.

Our validation study confirmed the general optimality of the PA-45 coil orientation towards the *fissura longitudinalis* (Brasil et al., 1992;

Mills et al., 1992). The slight deviations between the optima confirm the inter-individual variability in optimal coil orientation observed, for example, by Balslev et al. (2007) and Bungert et al. (2017).

4.2. Linking our results to simulations of neural excitation by TMS

Recent studies combined electric field simulations with compartment models of neurons. Seo et al. (2017) have proposed the initial segments of pyramidal cells, in layer 3 and 5, as the sites of primary excitation by TMS. In contrast, Aberra et al. (2018) found that the terminals of the axon collaterals, which are equally distributed in all directions around the main axon, have the lowest thresholds. Our results, namely high congruence factors of the overall magnitude and the magnitude of the tangential component of the electric field in the gyral crown and rim, indicate that the stimulation mechanism of TMS may indeed occur due to the dense collateralization in all directions of pyramidal cells and interneurons. This is in line with predictions from previous (Silva et al., 2008; Salvador et al., 2011) and very recent modeling studies (Aberra et al., 2020), providing a mechanistic explanation for our findings. Future studies may extend the congruence factor approach to more detailed neuronal models (Moezzi et al., 2018; Aberra et al., 2020) and tractography-based fiber tracts (De Geeter et al., 2015; De Geeter et al., 2016).

4.3. Factors influencing the stability of the results

The uncertainty and sensitivity analyses confirmed robust hotspots on the gyral crowns, extending to upper parts of the sulcal wall of M1 (see Fig. 10, Figs. S10–S12). The maxima of the means coincide well with the results of the deterministic case (see Fig. 9). The relative standard deviation (*RSD*) in the hotspots on the gyral crowns varied between 10 and 25%, depending on the subject. The uncertainties mainly translate into uncertainties of the congruence factor on the anterior sulcal wall of the precentral gyrus rather than the gyral crown, where the primary hotspot was detected.

The hotspots on the anterior sulcal wall lie in line with the normal vector of the head surface, towards the center of the brain. We hypothesize that these spurious hotspots are projections from the gyral crown hotspots. Since our approach is independent of the magnitudes of the electric field, but sensitive to their spatial profiles, these spurious hotspots might result from insufficient electric field variance between these locations.

Decomposing the variance by origin revealed a strong contribution from GM and WM conductivity as well as from the accuracy of the measured I/O curves. This is in line with previous studies, which showed that the electrical conductivity of GM and WM are the most influential parameters considering the induced electric field in grey matter (Weise et al., 2015; Codecasa et al., 2016; Saturnino et al., 2019). The impact of the measurement uncertainty was lower for subject Sub08 compared to the other subjects, which can be explained by the fact that the MEP curves could be determined with a higher certainty (Table 1, Table S1-S3). Nevertheless, its contribution was still high and special care should be taken when recording characteristic regions of the I/O curve, like the turning points of the sigmoids, to reduce its influence on the congruence factor. In contrast, the conductivity of CSF and the level of anisotropy had a small impact on the congruence factor and could be treated as deterministic in future analyses.

Note that, besides the factors that we investigated in our study, further potential sources of error include inaccurate segmentation, meshing, solving, and post-processing (Puonti et al., 2019a; Puonti et al., 2019b; Huang et al., 2019).

4.4. Towards a clinically suitable TMS mapping procedure

To enable clinical applicability of the proposed method, for instance in presurgical mapping, the experimental effort has to be reduced to a minimum while ensuring high reliability. Regarding our second research question, the permutation analysis from Experiment II (Fig. 8, Figs. S7–S9) revealed that six TMS conditions, at three different locations around M1, with different orientations are sufficient to address the localization problem at hand. Notably, the actual condition combinations that result in a minimum hotspot area differ strongly between subjects. This is likely due to inter-individual differences in anatomy and functional brain organization. Using a high number of experiments increases the stability and reliability of the solution. However, at the same time, it also reduces the resolution by introducing more measurement uncertainty. This became evident in the permutation study, in Fig. 8b, where the minimal hotspot area had a minimum for $k = 6$ conditions and slightly increased for higher values of k. Increasing the field variability is a promising starting point for subject-specific optimization to determine the optimal number and selection of coil positions and orientations before the experiment. An even more sophisticated scheme could involve maximizing the distinguishability between voxels based on their sensitivity profiles. A sensitivity profile of a voxel is defined as the vector of E fields caused by the different coil positions and orientations with identical stimulator intensity. It reflects how this particular E field value depends on the coil configuration. To distinguish two voxels with respect to their congruence factor, their sensitivity profiles should be as different as possible. Establishing an optimization procedure that identifies the best combination of coil positions and orientations to maximize the differences in the sensitivity profiles between any two voxels in the region of interest is a goal for future research.

Beyond the localization of the origin of MEPs, our approach allows the localization of cortical areas functionally involved in other processes, provided that it is possible to observe a quantitative response variable that depends on the TMS induced electric field strength. Considering adapted experimental paradigms, which are able to capture this, future studies may use our approach for pre-surgical language or somatosensory mapping purposes.

4.5. Study limitations

When using short inter stimulus intervals (ISI) like the 4 s we used in Experiment II, potential carry over effects might affect the I/O relationships. In our study, the ISI was kept constant during each experiment and the intensity of the TMS pulse was increased systematically and monotonically. Therefore, the correlative relationship between electric field and MEP amplitude should remain unaffected, even if the absolute value of the MEP is changed. This is corroborated by the observation that the results of subject Sub01 with different ISIs (4 and 5 s in Experiments I and II, respectively) are strikingly similar, and confirmed by the successful validation study.

Another potential limitation arises from the inhomogeneous distribution of the MEP variance over the I/O curve (heteroscedasticity). The variance is larger for the slope and upper saturation portions than for the lower saturation portion of the curve (Fig. 3b), which may have affected curve fitting. This problem could be ameliorated by a suitable data transformation, as suggested in the literature (Nielsen, 1996; Goetz et al., 2014). In fact, one could use sensitivity analysis as described in Section 3.4 to identify the data transformation that yields the smallest Sobol coefficient and therefore has the least impact on the congruence factor.

To compute E-MEP curves, the vector valued electric field needs to be converted into a scalar. This can be done by computing the magnitude in 3D ($|\mathbf{E}|$), by computing the magnitude within the tangential plane ($|\mathbf{E}_{||}|$), or by projecting onto a particular direction, in our case the cortex normal ($E_{\perp}$). In the latter case, the projection value can be positive or negative. Since we only used positive stimulator intensities in this study, each E-MEP curve based on the normal component covers either only positive or negative electric field values. As the excitability of cells potentially may depend on the field orientation, positive and negative curves occurring in one voxel cannot be compared directly. Therefore, we analyzed them separately (see *Supplementary Material* Section 1.2). A more rigorous

solution would be to use positive and negative intensities (by reversing the current direction) to obtain complete E-MEP curves, which can then be used to compute the congruence factor by using the shift approach in a straightforward way.

So far, our method relies on the assumption that the experimental effects can be explained by activity in a single cortical patch. This holds in the current motor experiment, identifying the cortical origin of FDI activation. In other experimental paradigms, however, several network nodes may exist that might influence the effect. These nodes may also influence each other in different ways, which would lead to partial correlations. Incorporating connections into our model will tremendously increase the computational cost and efficient algorithms will need to be developed to combine the electric field profiles and the physiological response data. Since numerous connections can be analyzed independently, the problem can be analyzed in parallel and is thus well suited for GPU or HPC implementations. The extension of our technique to identify multivariate relationships between externally observable effects and excitation of neural populations is subject of ongoing work.

Author contributions section

Konstantin Weise: Methodology, Software, Validation, Formal analysis, Investigation, Data Curation, Writing - Original Draft, Visualization, Project administration, Funding acquisition.

Ole Numssen: Methodology, Software, Validation, Formal analysis, Investigation, Data Curation, Writing - Original Draft, Visualization.

Axel Thielscher: Software, Conceptualization, Writing - Review & Editing, Supervision.

Gesa Hartwigsen: Conceptualization, Resources, Writing - Original Draft, Supervision, Project administration, Funding acquisition.

Thomas Knoesche: Conceptualization, Writing - Original Draft, Supervision, Project administration, Funding acquisition.

Acknowledgments

Konstantin Weise; Max Planck Institute for Human Cognitive and Brain Sciences, Stephanstr. 1a, 04103 Leipzig, Germany; Technische Universität Ilmenau, Advanced Electromagnetics Group, Helmholtzplatz 2, 98693 Ilmenau, Germany; e-mail: kweise@cbs.mpg.de, phone: +49 341 9940-2580. This work was partially supported by the German Science Foundation (DFG) (grant number WE 59851/1); Lundbeckfonden (grant no. R118-A11308), the NVIDIA Corporation (donation of two Titan Xp graphics cards to GH and KW) and NovoNordisk fonden (grant no. NNF14OC0011413).

Appendix A. Supplementary data

Supplementary data to this article can be found online at https://doi.org/10.1016/j.neuroimage.2019.116486.

References

Codecasa, L., Di Rienzo, L., Weise, K., Gross, S., Haueisen, J., 2016. Fast MOR-based approach to uncertainty quantification in transcranial magnetic stimulation. IEEE Trans. Magn. 52 (3), 7200904 https://doi.org/10.1109/TMAG.2015.2475120.

Aberra, A.S., Peterchev, A.V., Grill, W.M., 2018. Biophysically realistic neuron models for simulation of cortical stimulation. J. Neural Eng. 15 (6), 66023 https://doi.org/10.1088/1741-2552/aadbb1.

Aberra, A.S., Wang, B., Grill, W.M., Peterchev, A.V., 2020. Simulation of transcranial magnetic stimulation in head model with morphologically-realistic cortical neurons. Brain Stimul. 13 (1), 175–189. https://doi.org/10.1016/j.brs.2019.10.002.

Akaike, H., 1974. A new look at the statistical model identification. IEEE Trans. Autom. Control 19 (6), 716–723. https://doi.org/10.1109/TAC.1974.1100705.

Akhtari, M., Mandelkern, M., Bui, D., Salamon, N., Vinters, H.V., Mathern, G.W., 2010. Variable anisotropic brain electrical conductivities in epileptogenic foci. Brain Topogr. 23 (3), 292–300. https://doi.org/10.1007/s10548-010-0144-z.

Aonuma, S., Gomez-Tames, J., Laakso, I., Hirata, A., Takakura, T., Tamura, M., Muragaki, Y., 2018. A high-resolution computational localization method for transcranial magnetic stimulation mapping. Neuroimage 172 (1), 85–93. https://doi.org/10.1016/j.neuroimage.2018.01.039.

Balslev, D., Braet, W., McAllister, C., Miall, R.C., 2007. Inter-individual variability in optimal current direction for transcranial magnetic stimulation of the motor cortex. J. Neurosci. Methods 162 (1–2), 309–313. https://doi.org/10.1016/j.jneumeth.2007.01.021.

Baumann, S.B., Wozny, D.R., Kelly, S.K., Meno, F.M., 1997. The electrical conductivity of human cerebrospinal fluid at body temperature. IEEE Trans. Biomed. Eng. 44 (3), 220–223. https://doi.org/10.1109/10.554770.

Bestmann, S., 2008. The physiological basis of transcranial magnetic stimulation. Trends Cogn. Sci. 12, 81–83. https://doi.org/10.1016/j.tics.2007.12.002.

Bestmann, S., 2015. Computational neurostimulation in basic and translational research. Prog. Brain Res. 222, xv–xx. https://doi.org/10.1016/S0079-6123(15)00159-4.

Bestmann, S., Feredoes, E., 2013. Combined neurostimulation and neuroimaging in cognitive neuroscience: past, present, and future. Ann. N. Y. Acad. Sci. 1296, 11–30. https://doi.org/10.1111/nyas.12110.

Brasil, Neto, J.P., Cohen, L.G., Panizza, M., Nilsson, J., Roth, B.J., Hallett, M., 1992. Optimal focal transcranial magnetic activation of the human motor cortex: effects of coil orientation, shape of the induced current pulse, and stimulus intensity. J. Clin. Neurophysiol. 9 (1), 132–136 (PMID: 1552001).

Bungert, A., Antunes, A., Espenhahn, S., Thielscher, A., 2017. Where does TMS stimulate the motor cortex? Combining electrophysiological measurements and realistic field estimates to reveal the affected cortex position. Cerebr. Cortex 27, 5083–5094. https://doi.org/10.1093/cercor/bhw292.

Classen, J., Knorr, U., Werhahn, K.J., Schlaug, G., Kunesch, E., Cohen, L.G., Seitz, R.J., Benecke, R., 1998. Multimodal output mapping of human central motor representation on different spatial scales. J. Physiol. (Lond.) 512 (Pt 1), 163–179. https://doi.org/10.1111/j.1469-7793.1998.163bf.X.

Conforto, A.B., Z'Graggen, W.J., Kohl, A.S., Rösler, K.M., Kaelin-Lang, A., 2004. Impact of coil position and electrophysiological monitoring on determination of motor thresholds to transcranial magnetic stimulation. Clin. Neurophysiol. 115 (4), 812–819. https://doi.org/10.1016/j.clinph.2003.11.010.

Dale, A.M., Fischl, B., Sereno, M.I., 1999. Cortical surface-based analysis. I. Segmentation and surface reconstruction. Neuroimage 9 (2), 179–194. https://doi.org/10.1006/nimg.1998.0395.

Datta, A., Bikson, M., Fregni, F., 2010. Transcranial direct current stimulation in patients with skull defects and skull plates: high-resolution computational FEM study of factors altering cortical current flow. Neuroimage 52, 1268–1278. https://doi.org/10.1016/j.neuroimage.2010.04.252.

De Geeter, N., Crevecoeur, G., Leemans, A., Dupré, L., 2015. Effective electric fields along realistic DTI-based neural trajectories for modelling the stimulation mechanisms of TMS. Phys. Med. Biol. 60 (2), 453–471. https://doi.org/10.1088/0031-9155/60/2/453.

De Geeter, N., Dupré, L., Crevecoeur, G., 2016a. Modeling transcranial magnetic stimulation from the induced electric fields to the membrane potentials along tractography-based white matter fiber tracts. J. Neural Eng. 13 (2), 26028. https://doi.org/10.1088/1741-2560/13/2/026028.

De Geeter, N., Lioumis, P., Laakso, A., Crevecoeur, G., Dupre, L., 2016b. How to include the variability of TMS responses in simulations: a speech mapping case study. Phys. Med. Biol. 61 (21), 7571–7585. https://doi.org/10.1088/0031-9155/61/21/7571.

Fischl, B., Sereno, M.I., Dale, A.M., 1999. Cortical surface-based analysis. II: inflation, flattening, and a surface-based coordinate system. Neuroimage 9 (2), 195–207. https://doi.org/10.1006/nimg.1998.0396.

Fox, P.T., Narayana, S., Tandon, N., Sandoval, H., Fox, S.P., Kochunov, P., Lancaster, J.L., 2004. Column-based model of electric field excitation of cerebral cortex. Hum. Brain Mapp. 22, 1–14. https://doi.org/10.1002/hbm.20006.

Gabriel, C., Peyman, A., Grant, E.H., 2009. Electrical conductivity of tissue at frequencies below 1 MHz. Phys. Med. Biol. 54 (16), 4863–4878. https://doi.org/10.1088/0031-9155/54/16/002.

Ghanem, R., Higdon, D., Owhadi, H., 2016. Handbook of Uncertainty Quantification. Springer, Cham. https://doi.org/10.1007/978-3-319-12385-1.

Goetz, S.M., Luber, B., Lisanby, S.H., Peterchev, A.V., 2014. A novel model incorporating two variability sources for describing motor evoked potentials. Brain Stimul. 7 (4), 541–552. https://doi.org/10.1016/j.brs.2014.03.002.

Güllmar, D., Haueisen, J., Reichenbach, J.R., 2010. Influence of anisotropic electrical conductivity in white matter tissue on the EEG/MEG forward and inverse solution. A high-resolution whole head simulation study. Neuroimage 51 (1), 145–163. https://doi.org/10.1016/j.neuroimage.2010.02.014.

Hallett, M., 2000. Transcranial magnetic stimulation and the human brain. Nature 406, 147–150. https://doi.org/10.1038/35018000.

Hartwigsen, G., Bergmann, T.O., Herz, D.M., Angstmann, S., Karabanov, A., Raffin, E., Thielscher, A., Siebner, H.R., 2015. Modeling the effects of noninvasive transcranial brain stimulation at the biophysical, network, and cognitive Level. Prog. Brain Res. 222, 261–287. https://doi.org/10.1016/bs.pbr.2015.06.014.

Huang, Y., Datta, A., Bikson, M., Parra, L.C., 2019. Realistic volumetric-approach to simulate transcranial electric stimulation-ROAST-a fully automated open-source pipeline. J. Neural Eng. 16 (5), 56006. https://doi.org/10.1088/1741-2552/ab208d.

Jenkinson, M., Beckmann, C.F., Behrens, T.E., Woolrich, M.W., Smith, S.M., 2012. FSL NeuroImage 62 (2), 782–790. https://doi.org/10.1016/j.neuroimage.2011.09.015.

Krieg, T.D., Salinas, F.S., Narayana, S., Fox, P.T., Mogul, D.J., 2013. PET-based confirmation of orientation sensitivity of TMS-induced cortical activation in humans. Brain Stimul. 6 (6), 898–904. https://doi.org/10.1016/j.brs.2013.05.007.

Krieg, S., Tarapore, P.E., Picht, T., Tanigawa, N., Houde, J., Sollmann, N., Meyer, B., Vajkoczy, P., Berger, S.B., Ringel, F., Nagarajan, S., 2014. Optimal timing of pulse onset for language mapping with navigated repetitive transcranial magnetic stimulation. Neuroimage 100, 219–236. https://doi.org/10.1016/j.neuroimage.2014.06.016.

Laakso, I., Murakami, T., Hirata, A., Ugawa, Y., 2018. Where and what TMS activates: experiments and modeling. Brain Stimul. 11, 166–174. https://doi.org/10.1016/j.brs.2017.09.011.

Le Maitre, O.P., Knio, O.M., 2010. Spectral Methods for Uncertainty Quantification. Springer, Dordrecht. https://doi.org/10.1007/978-90-481-3520-2.

Li, C., Bak, A.F., Parker, L.O., 1968. Specific resistivity of the cerebral cortex and white matter. Exp. Neurol. 20 (4), 544–557. https://doi.org/10.1016/0014-4886(68)90108-8.

Logothetis, N.K., Kayser, C., Oeltermann, A., 2007. In vivo measurement of cortical impedance spectrum in monkeys: implications for signal propagation. Neuron 55 (5), 809–823. https://doi.org/10.1016/j.neuron.2007.07.027.

Mayka, M.A., Corcos, D.M., Leurgans, S.E., Vaillancourta, D.E., 2006. Three-dimensional locations and boundaries of motor and premotor cortices as defined by functional brain imaging. A meta-analysis. Neuroimage 31 (4), 1453–1474. https://doi.org/10.1016/j.neuroimage.2006.02.004.

Mills, K.R., Boniface, S.J., Schubert, M., 1992. Magnetic brain stimulation with a double coil: the importance of coil orientation. Electroencephalogr. Clin. Neurophysiol. Evoked Potentials 85 (1), 17–21. https://doi.org/10.1016/0168-5597(92)90096-T.

Moezzi, B.Schaworonkow N., Plogmacher, L., Goldsworthy, M.R., Hordacre, B., Mcdonnell, M., Iannella, N., Ridding, M.C., Triesch, J., 2018. Simulation of electromyographic recordings following transcranial magnetic stimulation. J. Neurophysiol. https://doi.org/10.1152/jn.00626.2017.

Nicholson, P.W., 1965. Specific impedance of cerebral white matter. Exp. Neurol. 13 (4), 386–401. https://doi.org/10.1016/0014-4886(65)90126-3.

Nielsen, J.F., 1996. Logarithmic distribution of amplitudes of compound muscle action potentials evoked by transcranial magnetic stimulation. J. Clin. Neurophysiol. 13 (5), 423–434. https://doi.org/10.1097/00004691-199609000-00005.

Nielsen, J.D., Madsen, K.H., Puonti, O., Siebner, H.R., Bauer, C., Madsen, C.G., Saturnino, G.H., Thielscher, A., 2018. Automatic skull segmentation from MR images for realistic volume conductor models of the head: assessment of the state-of-the-art. Neuroimage 174, 587–598. https://doi.org/10.1016/j.neuroimage.2018.03.001.

Oldfield, R.C., 1971. The assessment and analysis of handedness: the Edinburgh inventory. Neuropsychologia 9, 97–113. https://doi.org/10.1016/0028-3932(71)90067-4.

Opitz, A., Windhoff, M., Heidemann, R.M., Turner, R., Thielscher, A., 2011. How the brain tissue shapes the electric field induced by transcranial magnetic stimulation. Neuroimage 58, 849–859. https://doi.org/10.1016/j.neuroimage.2011.06.069.

Opitz, A., Legon, W., Rowlands, A., Bickel, W.K., Paulus, W., Tyler, W.J., 2013. Physiological observations validate finite element models for estimating subject-specific electric field distributions induced by transcranial magnetic stimulation of the human motor cortex. Neuroimage 81, 253–264. https://doi.org/10.1016/j.neuroimage.2013.04.067.

Opitz, A., Zafar, N., Bockermann, V., Rohde, V., Paulus, W., 2014. Validating computationally predicted TMS stimulation areas using direct electrical stimulation in patients with brain tumors near precentral regions. NeuroImage Clin. 4, 500–507. https://doi.org/10.1016/j.nicl.2014.03.004.

Pascual-Leone, A., Torres, F., 1993. Plasticity of the sensorimotor cortex representation of the reading finger in Braille readers. Brain 116 (1), 39–52 (PMID: 8453464).

Penny, W., Friston, K., Ashburner, J., Kiebel, S., Nichols, T., 2007. Statistical Parametric Mapping: the Analysis of Functional Brain Images, first ed. Academic Press (ISBN 9780123725608).

Picht, T., 2014. Current and potential utility of transcranial magnetic stimulation in the diagnostics before brain tumor surgery. CNS Oncol. 3 (4), 299–310. https://doi.org/10.2217/cns.14.25.

Puonti, O., Saturnino, G.B., Madsen, K.H., Thielscher, A., 2019a. Comparing and validating automated tools for individualized electric field simulations in the human head. bioRxiv, 611962. https://doi.org/10.1101/611962.

Puonti, O., Saturnino, G.B., Madsen, K.H., Thielscher, A., 2019b. Value and limitations of intracranial recordings for validating electric field modeling for transcranial brain stimulation. Neuroimage 116431. https://doi.org/10.1016/j.neuroimage.2019.116431.

Ranck, J.B., 1963. Specific impedance of rabbit cerebral cortex. Exp. Neurol. 7, 144–152. https://doi.org/10.1016/S0014-4886(63)80005-9.

Rossi, S., Hallett, M., Rossini, P.M., Pascual-Leone, A., 2009. Safety, ethical considerations, and application guidelines for the use of transcranial magnetic stimulation in clinical practice and research. Clin. Neurophysiol. 120, 2008–2039. https://doi.org/10.1016/j.clinph.2009.08.016.

Rossini, P.M., et al., 2015. Non-invasive electrical and magnetic stimulation of the brain, spinal cord, roots and peripheral nerves: basic principles and procedures for routine clinical and research application. An updated report from an IFCN Committee. Clin. Neurophysiol. https://doi.org/10.1016/j.clinph.2015.02.001.

Rothwell, J.C., Hallett, M., Berardelli, A., Eisen, A., Rossini, P., Paulus, W., 1999. Magnetic stimulation: motor evoked potentials. Electroencephalogr. Clin. Neurophysiol. Suppl. 52, 97–103 (PMID: 10590980).

Salinas, F.S., Szabó, C.Á., Zhang, W., Jones, L., Leland, M.M., Wey, H.Y., Duong, T.Q., Fox, P.T., Narayana, S., 2011. Functional neuroimaging of the baboon during concurrent image-guided transcranial magnetic stimulation. Neuroimage 57 (4), 1393–1401. https://doi.org/10.1016/j.neuroimage.2011.05.065.

Salvador, R., Silva, S., Basser, P.J., Miranda, P.C., 2011. Determining which mechanisms lead to activation in the motor cortex: a modeling study of transcranial magnetic stimulation using realistic stimulus waveforms and sulcal geometry. Clin. Neurophysiol. 122 (4), 748–758. https://doi.org/10.1016/j.clinph.2010.09.022.

Sandrini, M., Umilta, C., Rusconi, E., 2011. The use of transcranial magnetic stimulation in cognitive neuroscience: a new synthesis of methodological issues. Neurosci. Biobehav. Rev. 35, 516–536. https://doi.org/10.1016/j.neubiorev.2010.06.005.

Saturnino, G.B., Thielscher, A., Madsen, K.H., Knösche, T.R., Weise, K., 2019. A principled approach to conductivity uncertainty analysis in electric field calculations. Neuroimage 188 (1), 821–834. https://doi.org/10.1016/j.neuroimage.2018.12.053.

Saturnino, G.B., Madsen, K.H., Thielscher, A., 2019b. Electric field simulations for transcranial brain stimulation using FEM. An efficient implementation and error analysis. J. Neural Eng. 16 (6), 66032.

Seo, H., Schaworonkow, N., Jun, S.C., Triesch, J., 2017. A multi-scale computational model of the effects of TMS on motor cortex. F1000Res. 5, 1945. https://doi.org/10.12688/f1000research.9277.3, 2017.

Siebner, H.R., Hartwigsen, G., Kassuba, T., Rothwell, J.C., 2009. How does transcranial magnetic stimulation modify neuronal activity in the brain? Implications for studies of cognition. Cortex 45, 1035–1042. https://doi.org/10.1016/j.cortex.2009.02.007.

Silva, S., Basser, P.J., Miranda, P.C., 2008. Elucidating the mechanisms and loci of neuronal excitation by transcranial magnetic stimulation using a finite element model of a cortical sulcus. Clin. Neurophysiol. 119 (10), 2405–2413. https://doi.org/10.1016/j.clinph.2008.07.248.

Smith, S.M., Jenkinson, M., Woolrich, M.W., Beckmann, C.F., Behrens, T.E.J., Johansen-Berg, H., Bannister, P.R., De Luca, M., Drobnjak, I., Flitney, D.E., Niazy, R., Saunders, J., Vickers, J., Zhang, Y., De Stefano, N., Brady, J.M., Matthews, P.M., 2004. Advances in functional and structural MR image analysis and implementation as FSL. Neuroimage 23 (S1), 208–219. https://doi.org/10.1016/j.neuroimage.2008.10.055.

Sobol, I.M., 2001. Global sensitivity indices for nonlinear mathematical models and their Monte Carlo estimates. Math. Comput. Simulat. 55 (1–3), 271–280. https://doi.org/10.1016/S0378-4754(00)00270-6.

Sudret, B., 2008. Global sensitivity analysis using polynomial chaos expansions. Reliab. Eng. Syst. Saf. 93 (7), 964–979. https://doi.org/10.1016/j.ress.2007.04.002.

Tarapore, P.E., Findlay, A.M., Honma, S.M., Mizuiri, D., Houde, J.F., Berger, M.S., Nagarajan, S.S., 2013. Language mapping with navigated repetitive TMS: proof of technique and validation. Neuroimage 82, 260–272. https://doi.org/10.1016/j.neuroimage.2013.05.018.

Thielscher, A., Opitz, A., Windhoff, M., 2011. Impact of the gyral geometry on the electric field induced by transcranial magnetic stimulation. Neuroimage 54, 234–243. https://doi.org/10.1016/j.neuroimage.2010.07.061.

Thielscher, A., Antunes, A., Saturnino, G.B., 2015. Field modeling for transcranial magnetic stimulation: a useful tool to understand the physiological effects of TMS? Conf. Proc. IEEE Eng. Med. Biol. Soc. 222–225. https://doi.org/10.1109/EMBC.2015.7318340.

Tuch, D.S., Wedeen, V.J., Dale, A.M., George, J.S., Belliveau, J.W., 2001. Conductivity tensor mapping of the human brain using diffusion tensor MRI. Proc. Natl. Acad. Sci. U.S.A. 98 (20), 11697–11701. https://doi.org/10.1073/pnas.171473898.

Vorwerk, J., Cho, J.-H., Rampp, S., Hamer, H., Knösche, T.R., Wolters, C.H., 2014. A guideline for head volume conductor modeling in EEG and MEG. Neuroimage 100, 590–607. https://doi.org/10.1016/j.neuroimage.2014.06.040.

Wagner, T.A., Zahn, M., Grodzinsky, A.J., Pascual-Leone, A., 2004. Three-dimensional head model simulation of transcranial magnetic stimulation. IEEE Trans. Biomed. Eng. 51 (9), 1586–1598. https://doi.org/10.1109/TBME.2004.827925.

Weise, K., Di Rienzo, L., Brauer, H., Haueisen, J., Toepfer, H., 2015. Uncertainty analysis in transcranial magnetic stimulation using non-intrusive polynomial chaos expansion. IEEE Trans. Magn. 51 (7), 5000408 https://doi.org/10.1109/TMAG.2015.2390593.

Wenger, C., Salvador, R., Basser, P.J., Miranda, P.C., 2015. The electric field distribution in the brain during TTFields therapy and its dependence on tissue dielectric properties and anatomy: a computational study. Phys. Med. Biol. 60 (18), 7339–7357. https://doi.org/10.1088/0031-9155/60/18/7339.

Windhoff, M., Opitz, A., Thielscher, A., 2013. Electric field calculations in brain stimulation based on finite elements: an optimized processing pipeline for the generation and usage of accurate individual head models. Hum. Brain Mapp. 34, 923–935. https://doi.org/10.1002/hbm.21479.

Wolters, C.H., Anwander, A., Tricoche, X., Weinstein, D., Koch, M.A., MacLeod, R.S., 2006. Influence of tissue conductivity anisotropy on EEG/MEG field and return current computation in a realistic head model: a simulation and visualization study using high-resolution finite element modeling. Neuroimage 30 (3), 813–826. https://doi.org/10.1016/j.neuroimage.2005.10.014.

Woolrich, M.W., Jbabdi, S., Patenaude, B., Chappell, M., Makni, S., Behrens, T., Beckmann, C., Jenkinson, M., Smith, S.M., 2009. Bayesian analysis of neuroimaging data in FSL. Neuroimage 45 (S1), 173–186. https://doi.org/10.1016/j.neuroimage.2008.10.055.

Yedlin, M., Kwan, H., Murphy, J.T., Nguyen-Huu, H., Wong, Y.C., 1974. Electrical conductivity in cat cerebellar cortex. Exp. Neurol. 43 (3), 555–569. https://doi.org/10.1016/0014-4886(74)90195-2.

Zienkiewicz, O.C., Zhu, J.Z., 1992. The superconvergent patch recovery and aposteriori error estimates. Part 1: the recovery technique. Int. J. Numer. Methods Eng. 33 (7), 1331–1364. https://doi.org/10.1002/nme.1620330702.